JGR Solid Earth

RESEARCH ARTICLE
10.1029/2022JB024268

Earthquake Cycle Deformation Associated With the 2021 M_W 7.4 Maduo (Eastern Tibet) Earthquake: An Intrablock Rupture Event on a Slow-Slipping Fault From Sentinel-1 InSAR and Teleseismic Data

Jin Fang[1], Qi Ou[1,2], Tim J. Wright[1], Ryo Okuwaki[1,3,4], Ruth M. J. Amey[1], Tim J. Craig[1], John R. Elliott[1], Andy Hooper[1], Milan Lazecký[1], and Yasser Maghsoudi[1]

[1]COMET, School of Earth and Environment, University of Leeds, Leeds, UK, [2]COMET, Department of Earth Sciences, University of Oxford, Oxford, UK, [3]Mountain Science Center, University of Tsukuba, Tsukuba, Japan, [4]Faculty of Life and Environmental Sciences, University of Tsukuba, Tsukuba, Japan

Key Points:

- We present the earthquake cycle deformation for the 2021 Maduo earthquake from Sentinel-1 Interferometric Synthetic Aperture Radar and teleseismic waveforms
- Coseismic slip deficit is taken up by shallow and deep afterslip with different temporal behavior; this may be controlled by lithology
- Interseismic strain observed in the interior of a mapped tectonic block highlights importance of seismic hazard away from block boundaries

Supporting Information:

Supporting Information may be found in the online version of this article.

Correspondence to:

Q. Ou and J. Fang,
q.ou@leeds.ac.uk;
eejf@leeds.ac.uk

Citation:

Fang, J., Ou, Q., Wright, T. J., Okuwaki, R., Amey, R. M. J., Craig, T. J., et al. (2022). Earthquake cycle deformation associated with the 2021 M_W 7.4 Maduo (eastern Tibet) earthquake: An intrablock rupture event on a slow-slipping fault from Sentinel-1 InSAR and teleseismic data. *Journal of Geophysical Research: Solid Earth*, *127*, e2022JB024268. https://doi.org/10.1029/2022JB024268

Received 22 FEB 2022
Accepted 2 NOV 2022

Author Contributions:

Conceptualization: Tim J. Wright
Data curation: Jin Fang, Qi Ou, Milan Lazecký, Yasser Maghsoudi
Formal analysis: Jin Fang
Investigation: Jin Fang, Qi Ou, Ryo Okuwaki
Methodology: Jin Fang, Qi Ou, Ryo Okuwaki, Ruth M. J. Amey

Abstract In the continents, the importance of earthquakes that occur away from major block-bounding faults is still debated. The 21 May 2021 $M_W \sim 7.4$ Maduo earthquake occurred on a secondary fault away from previously-identified major block boundaries. Here we use 7 years of Sentinel-1 Interferometric Synthetic Aperture Radar (InSAR) time series (between October 2014 and November 2021) to determine the distribution of coseismic slip and early postseismic afterslip following the Maduo earthquake, and the preceding interseismic strain accumulation. We devised a 13-segment 3-D fault geometry constrained by the SAR range offsets and the distribution of relocated aftershocks and used a Bayesian method incorporating von Karman regularization to solve for coseismic slip and afterslip models. We also used teleseismic waveforms as a standalone inversion to show the rupture evolution in space and time during the earthquake, finding that it propagates bilaterally with three notable rupture episodes. Our preferred coseismic self-similar slip model shows a moderate shallow slip deficit, with the majority of moment release occurring in the depth interval of 1–10 km. The coseismic slip deficit is taken up in part by afterslip at shallow (<4 km) depths that grows linearly with time during the first ~6 months, and at >10 km depths where afterslip grows logarithmically with time. We suggest that this heterogeneity is likely controlled by spatial variations in fault friction related to lithology. We discuss the implications for seismic hazard away from major tectonic block boundaries in light of our observations of the earthquake cycle on this intrablock fault.

Plain Language Summary Collision between the Indian and Eurasian plates has created the largest deforming region on the planet. Part of the resultant deformation is accommodated by movements on block-bounding faults where major earthquakes usually occur. A large earthquake ruptured a slow-moving fault away from the major pre-identified block boundaries on 21 May 2021. We used 7 years of satellite radar images to measure the deformation that occurred before, during, and after the earthquake. We also used seismic observations to investigate the temporal evolution of the earthquake rupture. Our model agrees with the results from field mapping. Postseismic deformation at shallow and deep depths shows different temporally varying behavior, which is likely caused by the frictional properties of the fault associated with different physical characteristics of rocks. The causative fault was accumulating relatively subtle strain before the earthquake. We observed the strain being localized on one of the faults in the block interior, highlighting elevated earthquake potential in the future.

1. Introduction

It has been recognized that the continents do not deform like the oceans and continental deformation represents a significant departure from the kinematic rules of plate tectonics (England & McKenzie, 1982; Tapponnier & Molnar, 1976). However, the kinematics and dynamics of continental tectonics are still unclear. Despite decades of study, large continental earthquakes continue to surprise us, for example, by occurring in unexpected locations (e.g., the 2019 Ridgecrest earthquake sequence, Ross et al., 2019), or exhibiting remarkable complexity (e.g., the 2016 M_W 7.8 Kaikoura earthquake, Hamling et al., 2017). On 21 May 2021, a strong ($M_W \sim 7.4$) earthquake (referred to here as the Maduo earthquake) hit Maduo County in eastern Tibetan Plateau, rupturing a fault away from the main crustal block boundaries hypothesized for this region. We measure and model the coseismic,

Project Administration: Tim J. Wright, Tim J. Craig, John R. Elliott, Andy Hooper
Software: Qi Ou, Ryo Okuwaki, Ruth M. J. Amey
Supervision: Tim J. Wright, Tim J. Craig, John R. Elliott, Andy Hooper
Validation: Jin Fang, Qi Ou, Ryo Okuwaki
Visualization: Jin Fang, Qi Ou, Ryo Okuwaki
Writing – original draft: Jin Fang, Qi Ou, Ryo Okuwaki
Writing – review & editing: Jin Fang, Qi Ou, Tim J. Wright, Ryo Okuwaki, Ruth M. J. Amey, Tim J. Craig, John R. Elliott, Andy Hooper, Milan Lazecký, Yasser Maghsoudi

postseismic and interseismic deformation on the causative fault. This allows us to explore (a) the hazard of earthquakes in block interiors, (b) the role of geology in controlling frictional properties on faults, and (c) how strain rates vary through the earthquake cycle on a fault that is not a major block-bounding fault.

A popular approach for explaining continental deformation is to model the deformation as the motion of a number of blocks, or microplates, each following the kinematic rules of plate tectonics (Avouac & Tapponnier, 1993; Meade & Hager, 2005; McCaffrey et al., 2000; McClusky et al., 2001; Socquet et al., 2006; Thatcher, 2007; Wallace et al., 2004, 2005; W. Wang et al., 2017; Wang, Qiao, & Ding, 2021). They are useful in that they can help derive slip rates on major faults from geodesy (e.g., W. Wang, Qiao, & Ding, 2021; W. Wang et al., 2017). In most formulations of block models, no strain (and hence no earthquakes) occurs in the block interiors, although a few can account for internal strain (e.g., Q. Chen et al., 2004; Loveless & Meade, 2011). However, a number of earthquakes have occurred away from major block boundaries, for example, the 1947 M 7.7 Dari (eastern Tibet) earthquake (L. Liu, Li, et al., 2021), the 1992 M_W 7.3 Landers earthquake (Massonnet et al., 1993), the 1999 M_W 7.1 Hector Mine earthquake (Gomberg et al., 2001), the 2014 M_W 6.2 Ludian (southeastern Tibet) earthquake (Cheng et al., 2014), the 2019 Ridgecrest earthquakes (Ross et al., 2019), etc. It is noteworthy that the Landers/Hector Mine/Ridgecrest earthquakes occurred as a surprise to seismologists but geodetic strain within the Eastern California Shear Zone was visible before the events (Dokka & Travis, 1990a, 1990b). This raises the following key questions regarding earthquakes that occur in block interiors: What is the hazard from earthquakes in block interiors? Do earthquakes behave differently in continental interiors because of the relative structural immaturity of seismogenic faults, where the term structural maturity is used to describe the slip longevity of a fault (e.g., Manighetti et al., 2007, 2021; Perrin et al., 2016; Radiguet et al., 2009)? If Global Navigation Satellite System (GNSS) data are sparse, can Interferometric Synthetic Aperture Radar (InSAR) illuminate strain away from the main faults?

Tectonic strain can be accommodated in a variety of ways including through earthquakes and aseismic processes such as fault creep (Harris, 2017). Fault creep has been hypothesized to be controlled by the frictional resistance of specific rock materials as well as fault maturity/geometry and conditions on the fault such as temperature, fluid pressure, and stress state (Avouac, 2015; Byerlee & Brace, 1968; Collettini et al., 2009; Fagereng & Sibson, 2010; Gratier et al., 2011; Irwin & Barnes, 1975; Mavko, 1982; C. Marone, 1998; Reinen et al., 1991, 1992; Scholz, 1998; Thomas, Avouac, Champenois, et al., 2014; Thomas, Avouac, Gratier, & Lee, 2014; Wesson, 1988). Examples where lithology has been shown to play a role include the creeping section of the Longitudinal Valley Fault in Taiwan, which coincides with the clay-rich Lichi Mélang (Thomas, Avouac, Champenois, et al., 2014), the main creeping strand of the San Andreas Fault, which is related to abundant magnesium-rich clays revealed by deep drilling of borehole (Carpenter et al., 2012, 2015), and the creeping segment of the North Anatolian Fault, which is associated with lithologies that have low frictional strength (Cetin et al., 2014). The occurrence of postseismic afterslip following earthquakes and lack of shallow seismicity can also be explained by velocity-strengthening behavior of rocks in the uppermost crust (C. J. Marone et al., 1991; Shearer et al., 2005). Floyd et al. (2016) suggest the heterogeneity in the behavior of postseismic afterslip following the 2014 Napa earthquake is caused by spatial variations in fault friction linked to lithology. However, the number of cases where this has been documented is relatively small. By combining information from geological data with detailed models of coseismic slip and postseismic afterslip evolution, we can assess the role of lithological variations in controlling the frictional behavior of the Maduo earthquake.

Understanding how strain rates vary through an earthquake cycle is essential if we are to use short-term observations of present-day deformation to infer long-term slip rates on faults (Dolan et al., 2007; Elliott et al., 2016; Hussain et al., 2018; Khazaradze & Klotz, 2003; Nishimura, 2014; Salditch et al., 2020; Thatcher, 1993; Wright, 2016). Particularly powerful are observations of interseismic deformation that have been made prior to a major earthquake, whose coseismic and postseismic deformation are then observed (e.g., Hussain et al., 2016, 2018). However, only a handful of continental earthquakes have all three of these observations. For example, Elliott et al. (2016) found only 4 cases (i.e., the 1997 M_W 7.5 Manyi earthquake, the 1999 M_W 7.6 Izmit earthquake, the 2002 M_W 7.9 Denali earthquake, and the 2004 M_W 6.0 Parkfield earthquake), all of which were on major block-bounding faults. In all these cases, focused interseismic strain was observed prior to the earthquake, and this was followed by rapid postseismic deformation (Elliott et al., 2016; Hussain et al., 2018). The 2021 M_W 7.4 Maduo earthquake provides an opportunity to test whether this pattern exists also for major earthquakes that occur away from block-bounding faults.

It has been hypothesized that major active structures cut the Tibetan Plateau into several active tectonic blocks (Q. Chen et al., 2004; Loveless & Meade, 2011; Thatcher, 2007; W. Wang, Qiao, & Ding, 2021; W. Wang et al., 2017; P. Zhang et al., 2003; G. Zhang, Ma, et al., 2004) that play an important role in accommodating the crustal deformation and as a consequence control the spatial distribution of strong earthquakes (S. F. Chen et al., 1994; Q.-D. Deng et al., 2014; Wright et al., 2013; P.-Z. Zhang, 2013b). The Kunlun Fault (KF), the Longmenshan Fault, the Ganzi-Yushu-Xianshuihe Fault, and the western Altyn Tagh Fault define the boundaries of the Bayan Har Block (BHB) around which large earthquakes have struck frequently in recent decades. Such major events include the 1997 M_W 7.5 Manyi earthquake (Peltzer et al., 1999; Funning et al., 2007; Y.-Y. Wen & Ma, 2010), the 2001 M_W 7.8 Kokoxili earthquake (Lasserre et al., 2005; Ozacar & Beck, 2004; Walker & Shearer, 2009), the 2008 M_W 7.9 Wenchuan earthquake (Shen et al., 2009; Q. Wang et al., 2011; P.-Z. Zhang, 2013a), the 2010 M_W 6.9 Yushu earthquake (Z. Li et al., 2011), the 2013 M_W 6.6 Lushan earthquake (Y. Li, Jia, et al., 2014), and the 2017 M_W 6.5 Jiuzhaigou earthquake (X.-W. Xu et al., 2017) (Figure 1a). The 2021 M_W 7.4 Maduo earthquake ruptured a secondary fault within the BHB, ∼70 km south of the KF. The seismogenic fault, the Jiangcuo Fault, was previously identified in the database of active faults from Q. Deng et al. (2003). However, it had received little attention before the occurrence of the 2021 Maduo earthquake due to the absence of large earthquakes. Among all the block models of Tibet (Q. Chen et al., 2004; Loveless & Meade, 2011; Thatcher, 2007; W. Wang, Qiao, & Ding, 2021; W. Wang et al., 2017), the Jiangcuo Fault has never been defined as a block boundary, including the most recently published 30-element block model for Tibet (W. Wang et al., 2017) (Figure 1c). Geodetic observations from GNSS reveal that the fault is slow-moving, with a maximum slip rate of less than 2 mm/yr (Guo et al., 2021; Y. Zhu, Diao, et al., 2021), exhibiting a relatively low interseismic strain rate either from GNSS (20–30 nanostrain/yr, M. Wang, Shen, et al., 2021; M. Wang, Wang, et al., 2021) or InSAR (<20 nanostrain/yr, Zhao et al., 2021); both show a distributed deformation around the fault. A very slow slip rate of ∼0.6 mm/yr (strike-slip) has been estimated geologically (Pan et al., 2022).

In this study, we conduct a comprehensive analysis of geodetic observations of earthquake cycle deformation for the 2021 M_W 7.4 Maduo earthquake. We use Sentinel-1 InSAR data to investigate the coseismic deformation and time series of postseismic deformation occurring in the first ∼6 months following the Maduo earthquake. We apply a Bayesian method incorporating self-similarity to solve for coseismic slip and early afterslip models. We also analyze the rupture evolution by incorporating teleseismic data. In addition, we characterize the interseismic strain accumulation by combining Sentinel-1 InSAR and GNSS data. We further evaluate Coulomb stress loading caused by the Maduo earthquake. We discuss the lithological contrasts around the fault which likely control the fault slip behavior and the implications of our findings for the seismic hazard of low-slip-rate faults in "block" interiors.

2. Data and Methods

2.1. InSAR Data and Processing

Lazecký et al. (2020) developed an operational system based on the GAMMA software (Wegnüller et al., 2016), referred to as "Looking into Continents from Space with Synthetic Aperture Radar" (LiCSAR), to produce large-scale Sentinel-1 interferograms and derived products automatically for tectonic and volcanic areas. We used this system to process Sentinel-1 satellite data from ascending track 99 and descending track 106 for all epochs from 2021/05/20 to 2021/11/28. Interferograms were generated between each epoch and four preceding and/or following epochs. The coherence was calculated by 5 × 5 window convolution over interferograms multilooked by 20/4 pixels in range/azimuth direction. We then geocoded and exported it to 8-bit datatype. The values of the derived coherence vary between 0 and 255 where 0 refers to the lowest coherence and 255 indicates the highest value of coherence. We used single shortest interferogram pairs to capture the coseismic signals. The earliest acquisition after the earthquake was on 2021/05/26, meaning that the data contain 5 days of postseismic signal in addition to coseismic deformation (Figure 2). The interferogram unwrapping was performed using the Statistical-cost, Network-flow Algorithm for Phase Unwrapping approach (C. W. Chen & Zebker, 2000, 2001, 2002), with Gaussian-filtered pixel offsets in the SAR range direction as a coarse estimate to guide the unwrapping for coseismic interferograms, considering high deformation gradients in the near field that cause decorrelation of the radar phase. We then built small baseline networks (Figure S1 in Supporting Information S1) to analyze the postseismic time series. To investigate the tectonic strain accumulation in this region, we processed data from 5 ascending and 5 descending LiCSAR frames each covering approx. 250 × 250 km^2 area

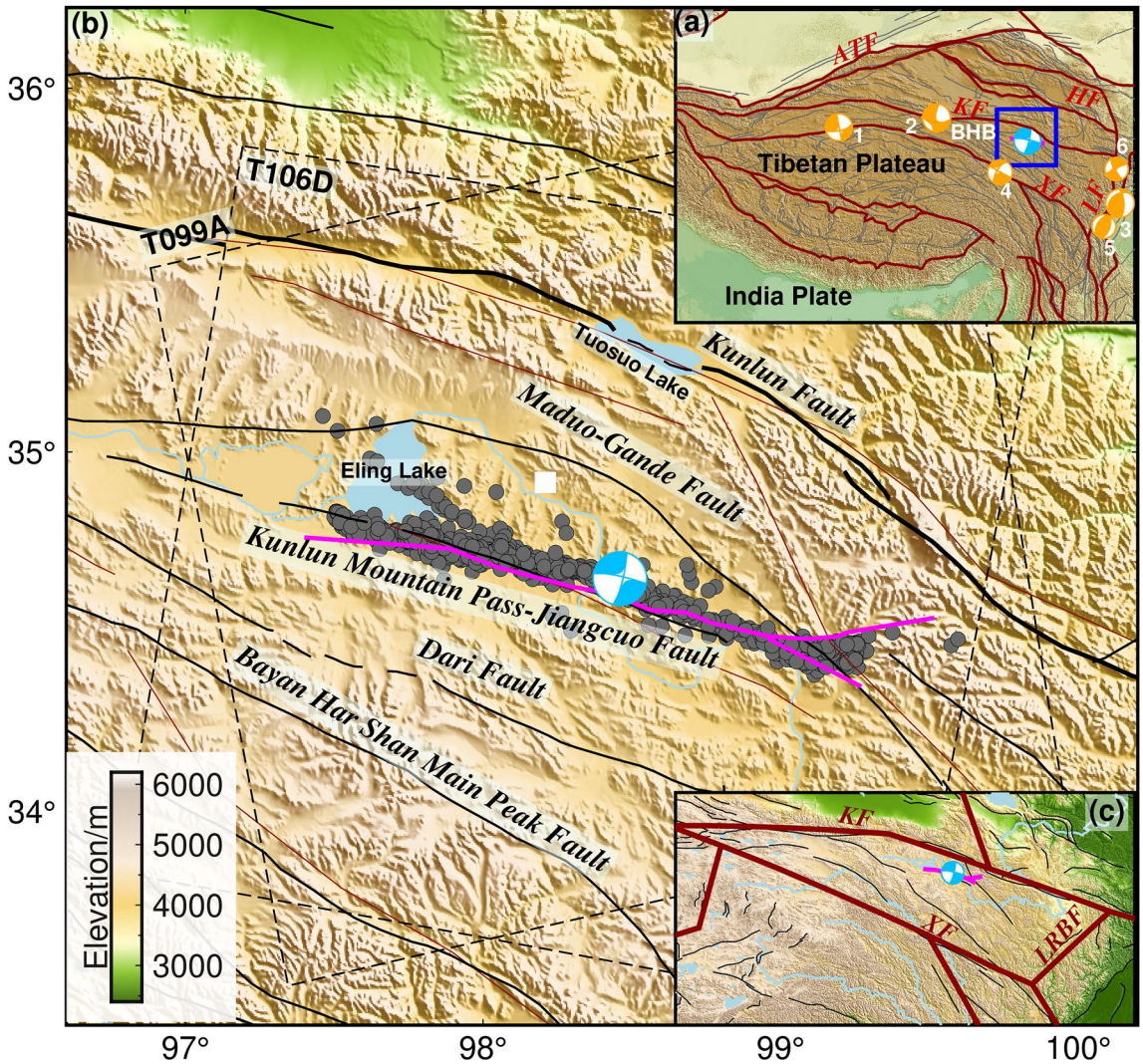

Figure 1. Tectonic setting of the 2021 Maduo earthquake. (a) The early definition of active tectonic blocks in Tibet (P. Zhang et al., 2003). Gray lines depict fault traces from Q. Deng et al. (2003). Blue beach ball marks the epicenter of the Maduo earthquake while orange ones are several large earthquakes occurring around the BHB in recent years. (b) The close-up for the blue rectangle in (a). Thick black lines show fault traces from Q. Deng et al. (2003). Thin dark red lines show fault traces from the Global Earthquake Model Global Active Faults Database (Styron & Pagani, 2020). White square represents Maduo County. Beach ball shows the location and focal mechanism of the earthquake from the Global Centroid Moment Tensor (GCMT) catalog (Dziewonski et al., 1981; Ekström et al., 2012). Gray dots are 8 days of relocated aftershock sequence (W. Wang, Fang, et al., 2021). Magenta lines depict the traces of surface rupture delineated from the SAR range offsets and are used to constrain the strike and location of the fault for slip inversion. Dashed-line polygons delimit the spatial extents of Sentinel-1 InSAR data used for coseismic deformation analysis in this study. (c) Block boundaries from W. Wang et al. (2017) shown as thick dark red lines. Black lines depict active faults compiled by Taylor and Yin (2009). Beach ball marks the epicenter of the 2021 Maduo earthquake and magenta lines show the surface rupture traces. ATF = Altyn Tagh Fault, HF = Haiyuan Fault, KF = Kunlun Fault, LF = Longmenshan Fault, XF = Ganzi-Yushu-Xianshuihe Fault, LRBF = Longriba Fault, BHB = Bayan Har Block. Beach ball 1 = 1997 M_W 7.5 Manyi earthquake, 2 = 2001 M_W 7.8 Kokoxili earthquake, 3 = 2008 M_W 7.9 Wenchuan earthquake, 4 = 2010 M_W 6.9 Yushu earthquake, 5 = 2013 M_W 6.6 Lushan earthquake, 6 = 2017 M_W 6.5 Jiuzhaigou earthquake.

since October 2014 until a pre-earthquake date in May 2021. The interseismic interferogram networks can be found in Figure S2 in Supporting Information S1.

To account for the covariance of atmospheric noise, we used the semi-variogram method (e.g., Lohman & Simons, 2005) to calculate a variance-covariance matrix for InSAR data. We selected an undeforming area of the interferogram and calculated the semi-variogram and the exponential fit (Figure S3 in Supporting Information S1), assuming that errors in the InSAR data can be simulated using an exponential function fitted to the isotropic experimental semi-variogram (Webster & Oliver, 2007). We downsampled the data by using a nested

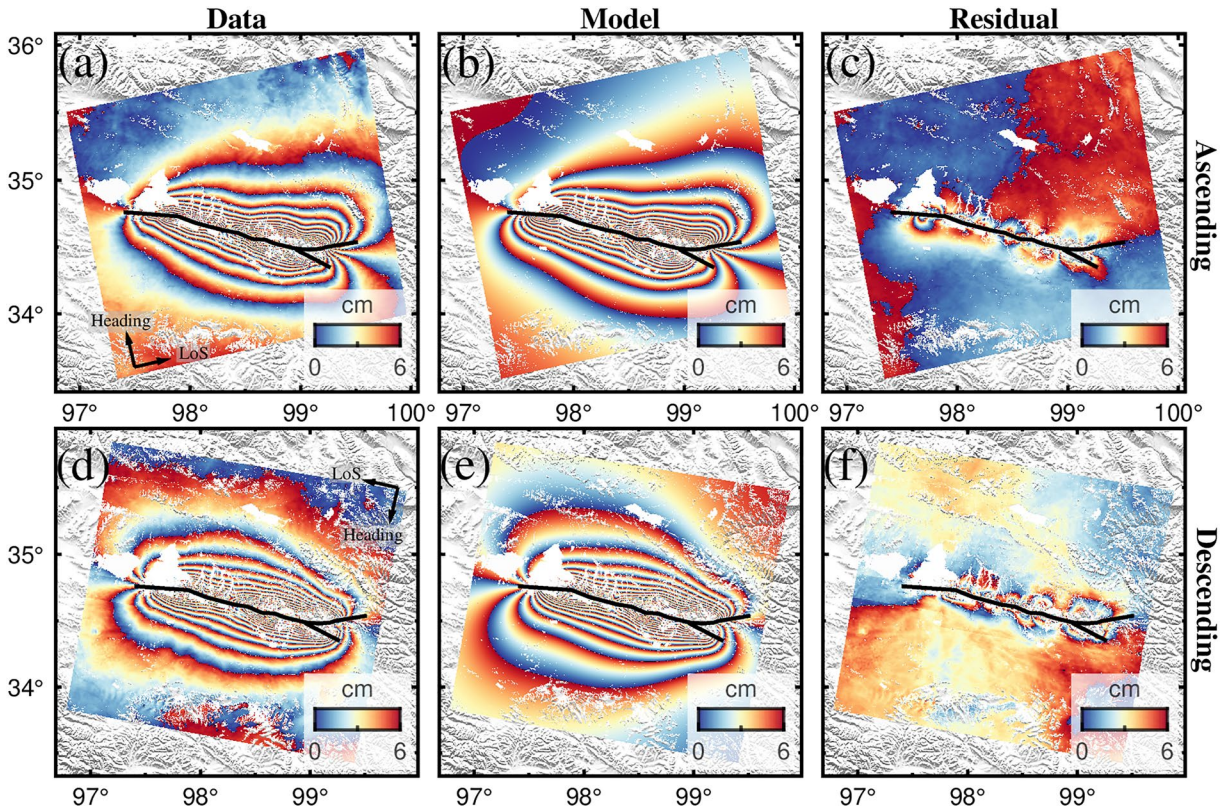

Figure 2. Observed (a, d), model (b, e), and residual (c, f) interferograms (2021/05/20–2021/05/26) for the Maduo earthquake. Each color cycle equals 6 cm of ground displacement toward the satellite. Black lines are surface rupture traces.

uniform downsampling method; we used around 3,000 points for both ascending and descending InSAR viewing geometries for the inversion of fault slip (Figure S4 in Supporting Information S1).

2.2. InSAR Time Series Analysis

Morishita et al. (2020) presented an open-source InSAR time series analysis package, referred to as LiCSBAS, which integrates with LiCSAR products, facilitating large scale processing (Morishita, 2021; Weiss et al., 2020). We inverted for displacement time series using LiCSBAS software. We processed each frame at a resolution of ~100 m. We performed the GACOS correction (Yu et al., 2018) to reduce atmospheric noise contributions to the time series. The range of coherence is converted to 0–1 in LiCSBAS processing. Low coherent pixels (average coherence $\leq$0.1) were masked before time series inversion, as in Morishita (2021). This is a safe mask as we do not intend to exclude too many pixels. Cumulative postseismic displacements were derived from spatiotemporal filtered time series, with a temporal filter width of 0.05 years and a spatial filter width of 1 km. The LiCSBAS parameter settings used in this study were listed in Table S1 in Supporting Information S1.

F. Liu, Elliott, et al. (2021) presented a time series approach to extract a linear interseismic rate, a coseismic offset, and a postseismic relaxation function. However, this assumes the postseismic deformation of each pixel follows a logarithmic function with a constant decay parameter (τ) to represent the postseismic relaxation for the region. This is not optimal for studies in which postseismic afterslip can be linear and logarithmic through time at different spatial locations (e.g., Floyd et al., 2016).

2.3. Teleseismic Waveform Data

To analyze the rupture evolution during the 2021 Maduo earthquake, we use vertical-component teleseismic *P* waveforms from 53 globally distributed stations. The data are selected to ensure good azimuthal coverage of high-quality records, with high signal-to-noise ratios that are sufficient for reliable picks of the *P*-wave first

motions (Okuwaki et al., 2016). The first motions are manually determined. The data are then deconvolved from instrument responses into velocity time series at a sampling interval of 0.8 s.

2.4. Von Karman Regularized Geodetic Bayesian Slip Inversion

2.4.1. Fault Geometry Set Up

Before the inversion, the strike angles of the fault were fixed based on the trace of fault rupture delineated from the SAR range offsets which indicate a 156 km long surface rupture with a single major trace along most of length except in the east where there is a secondary sub-parallel splay (Figure S5 in Supporting Information S1). The dip angles for different segments were determined based on the relocated aftershocks, which suggest a near-vertical but complex geometry, dipping to north or south in different strands (W. Wang, Fang, et al., 2021). The relocated aftershocks are of ∼0.3 km average accuracy in horizontal and of ∼0.5 km in depth. Our resultant 3-D fault geometry has 13 planar segments with different strike and dip angles (Table S2 in Supporting Information S1). Each segment is fully connected at surface. To compensate for the poorer fault resolution at depth (e.g., Lohman & Simons, 2005), we use a variable patch size, increasing from ∼1 km at the top, ∼3 km at 1–4 km depth, ∼6 km at 4–10 km depth, to ∼10 km at the bottom (Figure 3). We make the slip patches square as possible, within the constraints of the lengths of the planar segments.

2.4.2. Coseismic Slip Inversion

We applied a Bayesian method incorporating von Karman regularization to solve for slip distribution at depth and associated standard deviation (Amey et al., 2018). Von Karman smoothing is arguably more physically meaningful than Laplacian smoothing, as it accounts for fractal (self-similar) properties of fault slip as evidenced by Aviles et al. (1987), Robertson et al. (1995), Mai and Beroza (2002), Ben-Zion (2008), Powers and Jordan (2010), and Passelègue et al. (2016). Practically, the von Karman solution outperforms the Laplacian solution in that the former gives tighter confidence bounds on slip, as shown in Amey et al. (2018). Once the fault geometry has been determined (Section 2.4.1), we solve for slip and rake angle for each patch using the slipBERI code (Amey et al., 2018), as well as a hyperparameter α^2 controlling the slip variance for each separate fault. Thus, we can explore the full range of solutions for a range of variances, instead of assuming the variance of slip in advance. The initial slip value for each patch was assigned 0.4 m and the maximum slip allowed was 10 m. During the inversion, rake angles were allowed to vary from −60° to 60°, reflecting the predominant left-lateral strike-slip motion but also allowing for a variable dip-slip component of slip. The initial probability target (i.e., the expected ratio of the posterior probability after perturbation of a single model parameter, to the current posterior probability) was 10^{-4}, which was used to adjust step sizes in the initial part of the inversion. We applied von Karman smoothing including patches in connected fault segments. Details about this approach are given in Amey et al. (2018).

2.4.3. Postseismic Afterslip Inversion

We apply the same scheme as coseismic slip inversion to obtain early afterslip models over 6 time intervals (∼1, ∼2, ∼3, ∼4, ∼5, and ∼6 months after the mainshock), using the cumulative postseismic displacements from the filtered postseismic time series as input, sampled at the same locations as the coseismic inversion. To mitigate the long-wavelength disturbance, we remove a best-fit ramp before inversion. We then investigate the time-dependent afterslip behavior in the first ∼6 months following the Maduo earthquake.

Jin and Fialko (2021a) suggest that the viscoelastic relaxation in the first 6 months following the Maduo earthquake might be limited. Calculating a specific viscosity is difficult without a comprehensive viscoelastic modeling study, which is beyond the scope of this study. The viscosity depends on the geometry of the region responding, the type of viscoelasticity (e.g., linear Maxwell or power-law), and whether viscoelastic relaxation is the only process occurring. Also, we note that it is difficult to distinguish between deep afterslip and viscoelastic processes based on geodetic measurements, because deep aseismic slip in an elastic half-space can produce the equivalent surface deformation as that produced by viscoelastic relaxation (Savage, 1990). We note, however, that any deep postseismic afterslip may in reality be accommodated by viscoelastic processes.

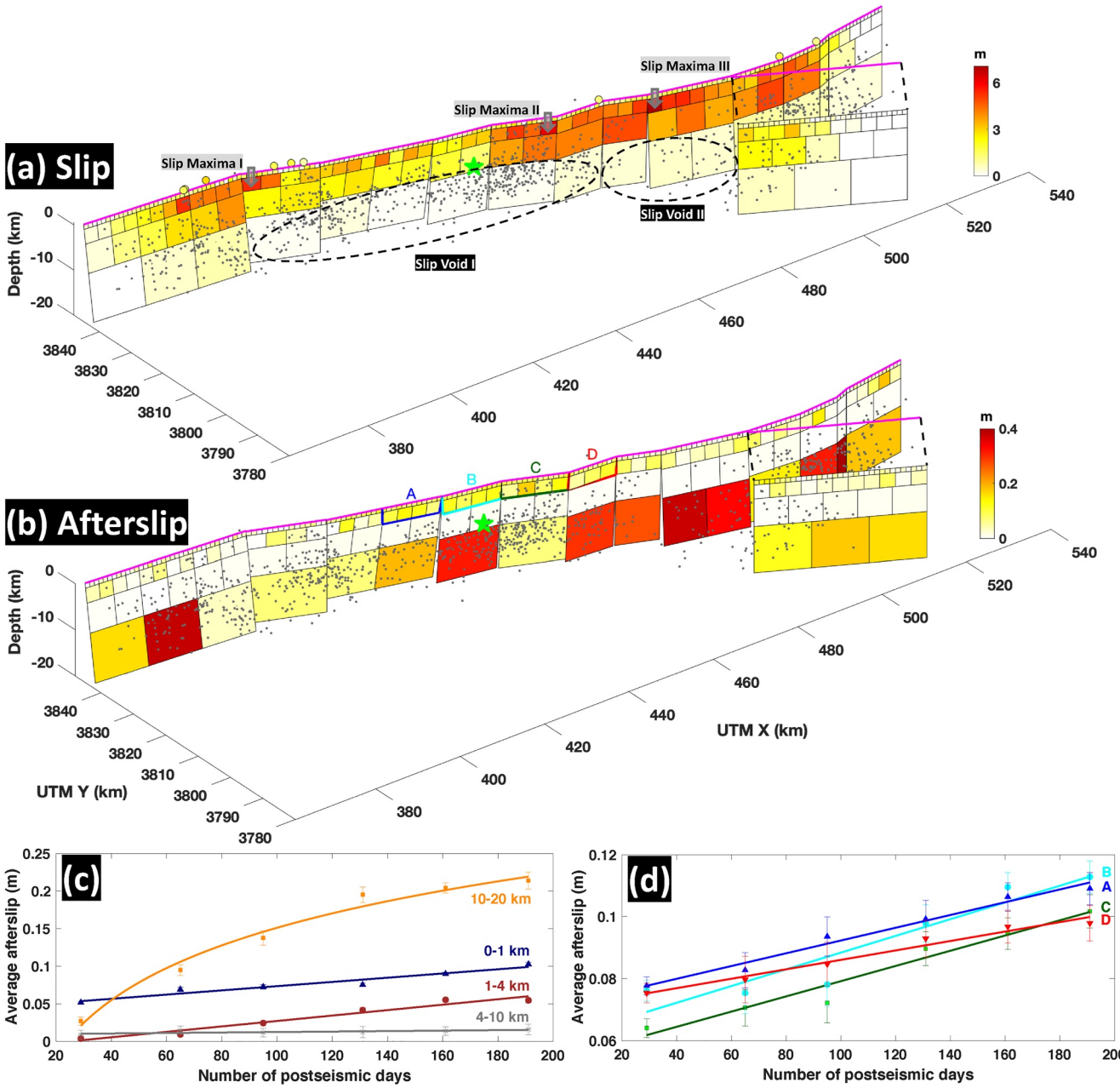

Figure 3. (a) Coseismic slip model (containing 5-day postseismic afterslip) for the Maduo earthquake. Magenta lines represent the traces of surface rupture. For a better visualization, the splay at the eastern end was shifted by an arbitrary amount to the south-west. Yellowish circles show the left-lateral offsets from field surveys (Z. Li et al., 2021; Pan et al., 2021), which share the same color scale with slip patches. Green star marks the hypocenter and gray dots are 8 days of relocated aftershocks (W. Wang, Fang, et al., 2021). (b) Afterslip distribution occurring in the first ~6 months (2021/05/26–2021/11/28). (c) Temporal evolution of average afterslip for each depth range. Lines show linear fitting and logarithmic fitting with a functional form of "$y = a * \log(1 + b*t) + c$." (d) Same as (c), but for shallow patches delimited by polygons A, B, C, and D shown in (b).

2.5. Teleseismic Finite-Fault Inversion

2.5.1. Fault Geometry Configuration

Guided by the SAR range offsets of the surface deformation, we design a non-planar model domain for the teleseismic finite-fault inversion. The model domain is defined with variable strike and fixed dip angles (90°). The model space covers ~165 km in length and 25 km in width. During our teleseismic finite-fault inversion, we omit the branching fault elongated toward southeast, closely co-located with the eastern part of the model domain,

because the spatial gap between the main fault strand and the branch is too close to be resolved by the limited spatial resolution of the teleseismic data. Each patch is defined to be 5×5 km^2 along the strike and dip directions. Given the observed surface ruptures, the model edges are constrained to taper to zero except for the upper surface.

2.5.2. Green's Functions Calculation

We use the ak135 model (Kennett et al., 1995) to calculate relative travel times, ray parameter, and geometric spreading factors. Green's functions are calculated based on the ray-theory approach (Kikuchi & Kanamori, 1991). The CRUST1.0 model (Laske et al., 2013) is used to extract a one-dimensional layered velocity model near the source region to calculate Haskel propagator in Green's functions. We do not apply a low-pass filter to both the observed waveforms and Green's functions, which is intended to retrieve the detailed rupture process recorded in higher frequency components, following the procedure adopted in previous studies (e.g., Okuwaki et al., 2021; Shimizu et al., 2020).

2.5.3. Finite-Fault Rupture Evolution Inversion

We use a finite-fault inversion method based on the potency-density tensor approach (Shimizu et al., 2020; Yagi & Fukahata, 2011). This method considers the uncertainty of the Green's functions by adopting the formulation of Yagi and Fukahata (2011), which explicitly introduces the error term of the Green's functions into the data covariance matrix. The method also accounts for the uncertainty of fault geometry by representing the fault deformation by a superposition of five basis double-couple components (Kikuchi & Kanamori, 1991), which solves a spatiotemporal distribution of potency density (Ampuero & Dahlen, 2005).

During the inversion, the slip-rate function for each source grid is represented by linear B-splines at a temporal interval of 0.8 s. The duration of slip-rate function is set as 20 s. The maximum rupture velocity is set as 5 km/s so that we can flexibly determine a slip evolution including a possible supershear rupture. We set the hypocenter at 34.618°N, 98.387°E, and 12.5 km at depth for the initial rupture point, which is slightly shifted from the relocated earthquake origin (W. Wang, Fang, et al., 2021) so that the initial rupture point is located within the determined fault "plane" (Section 2.5.1). In order to evaluate the sensitivity of our teleseismic finite-fault inversion against the assumption of the initial rupture point, we testify different scenarios of the initial rupture point near the USGS and W. Wang, Fang, et al. (2021)'s reported hypocenters, and in between. We find the variance between the observed and synthetic waveforms is similar (within ~1% difference) among the solutions (Figure S6 in Supporting Information S1).

The model parameters are objectively determined by minimizing Akaike's Bayesian Information Criterion (ABIC) (Akaike, 1980; Yabuki & Matsu'ura, 1992), and we do not adopt non-negative constraints for slip vectors. Such a procedure can effectively prevent over- or under-smoothing of the source model as theoretically shown in Fukuda and Johnson (2008). Thus, our method is data-driven and designated to retrieve the information of slip direction and rupture evolution recorded in the teleseismic data, instead of biasing the solution by the prescribed fault geometry and slip vectors. The potency-density tensor approach of the finite-fault inversion (Shimizu et al., 2020) adopted in this study has been proven efficient to flexibly model complex rupture evolution of large earthquakes (Hicks et al., 2020; Okuwaki et al., 2020, 2021; Tadapansawut et al., 2021; Yamashita et al., 2021), which is suitable for estimating the non-smooth rupture propagation in geometrically complex fault systems.

2.6. Interseismic LOS Velocity Mosaicking and Strain Rate Calculation

2.6.1. LiCSAR Frame Mosaicking

To mosaic the independently referenced frames of line-of-sight (LOS) velocities along track, we used a method developed by Ou et al. (2022) where a planar ramp per frame is jointly inverted from both the differences between InSAR LOS and GNSS LOS velocities and the differences between InSAR LOS velocities in the overlapping bursts between consecutive frames. GNSS velocities are from Liang et al. (2013) and M. Wang and Shen (2020). The vertical velocities in Liang et al. (2013) were measured before the start of our InSAR time series and could be impacted by fluctuations coming from hydrological processes. However, since Liang et al. (2013) is so far the only source of vertical GNSS velocities published for the region, and knowing that treating GNSS vertical velocities as zero could equally bias the results, we incorporated the vertical velocities from Liang et al. (2013) and weighted the inversion by the combined uncertainties from those of the InSAR and GNSS LOS velocities.

This weighting strategy produces better fits at GNSS stations with more stable vertical velocities. The average residuals of -0.2 ± 1.7 mm/yr between InSAR and GNSS LOS (Figure S7 in Supporting Information S1) and -0.8 ± 2.3 mm/yr between InSAR frame overlaps (Figure S8 in Supporting Information S1) suggest that the stitched LOS tracks are of ~1–2 mm/yr uncertainty level. This procedure places the InSAR LOS velocities into a common reference frame provided by the GNSS velocities (Figure S9 in Supporting Information S1).

2.6.2. LOS Velocity Decomposition

To extract regional east and vertical velocity fields from the 3 ascending and 3 descending LOS velocity tracks, we first remove the contributions of the GNSS estimated north velocities from the LOS, and then decompose the remaining LOS velocities into east and vertical components (Hussain et al., 2018; Weiss et al., 2020). The velocity decomposition is weighted by LOS uncertainties corrected for the effect of frame reference. This is done by scaling the LOS uncertainties by a factor determined by a spherical model fitted to an uncertainty profile against the distance away from the median location of pixels with the lowest 3% uncertainties (Figure S10 in Supporting Information S1, Ou et al., 2022). The north velocity field was interpolated from GNSS north velocities using a universal kriging algorithm provided by version 1.6.1 of the PyKrige Python Package (Murphy et al., 2021). The kriging algorithm generates the best linear unbiased predictions at unsampled locations as weighted means of neighboring GNSS velocities. The weights are distance-dependent and derived from a variogram model fitted to the semi-variogram of the deviations of the data from a polynomial trend. We chose to fit a spherical instead of an exponential or Gaussian variogram model to balance smoothness and feature retention (Ou et al., 2022). To avoid artifacts due to closely-spaced contrasting velocities of mixed quality, we interpolated only GNSS north velocities with uncertainties below 0.7 mm/yr. The kriging algorithm also uses the same variogram model to produce interpolated uncertainties that increase away from the GNSS control points. We propagate the uncertainties of the interpolated GNSS north velocities through the LOS velocity decomposition by compounding the V_N uncertainties with the LOS uncertainties as described in the Supporting Information S1 of Ou et al. (2022). The two velocity fields we obtained are of ~100 m resolution, 1–2 mm/yr uncertainty, and spans an area of 205,000 km^2 (Figures S11 and S12 in Supporting Information S1). The correlations between InSAR and GNSS V_E and V_U have slopes of 0.94 and 0.76, and R^2 values of 0.98 and 0.93, respectively (Figures S11g and S11h in Supporting Information S1).

2.6.3. Strain Rate Calculation

We further investigate the degree to which the earthquake here is spatially associated with the recent prior accumulation of strain in the immediate region and the degree to which this strain is concentrated on the fault. We generate strain rate fields at 1 km sampling spacing using average velocities derived from ~6.5 years of Sentinel-1 InSAR time series (between October 2014 and May 2021, see Figure S2 in Supporting Information S1 for the interferogram networks). We follow the method of Ou et al. (2022) to derive strain rate fields by combining horizontal velocity gradients of the filtered InSAR east velocities and the interpolated GNSS north velocities (Section 2.6.2, Figure S13 in Supporting Information S1).

The InSAR east velocities are filtered with a sliding median filter of 60 km diameter, as in Ou et al. (2022). In areas of high pixel densities, the filtered east velocity represents the median value of up to >250,000 V_E measurements in a circular window, effectively reducing the bias from extreme values typically found near decorrelated regions. Besides, a median filter preserves the shapes of the velocity profile and hence the width of the strain rate peak. If the pixels are unevenly distributed within a circle, the median value can be more representative of the velocity from a side with higher pixel density. As a result, the filter may smear velocities from two sides of a decorrelated patch toward its geometric center where potentially different velocities meet in a sharp velocity step. This may give rise to a strain rate peak that is too narrow and spiky because the velocity gradient is poorly constrained. If the pixel distribution is asymmetrical about a fault, the filter may cause a spatial drift of the strain rate peak away from the fault toward the side of lower pixel density. However, the spatial drift or shape change of the strain rate peak does not affect the total strain rate integrated along a profile or across a region, and any strain rate peak highlighted is indicative of a real velocity contrast that is worth interpreting with reference to the unfiltered V_E. Such limitations could be mitigated using a Bayesian approach (e.g., Pagani et al., 2021), although the number of InSAR measurements could make such a method computationally expensive to implement.

3. Results

3.1. Coseismic Slip Model

The 2021 Maduo earthquake is a predominantly left-lateral strike-slip event. Figure 3 shows our preferred self-similar slip model through the implementation of a von Karman regularization. The rupture propagated bilaterally with a total length of ~160 km, resulting in two major individual slipping areas distributed separately to the west and east of the hypocenter; the central part produced relatively minor slip (30% below average), consistent with the results of Jin and Fialko (2021b), K. He, Wen, et al. (2021), and J. Liu et al. (2022). The maximum slip is ~7 m, located at depth of 1–4 km to the east of the hypocenter. Geometric barriers have been proposed to hinder or terminate the rupture propagation during small-to-moderate-sized earthquakes and fail only during large-magnitude earthquakes on mature faults (e.g., Manighetti et al., 2007). Our slip model shows multi-peak slips occur at fault segment junctions (i.e., gray arrows denoting slip maxima in Figure 3a), which appear to be associated with geometric barriers. This echoes the finding of M. Wang, Wang, et al. (2021). A similar rupture scenario was proposed for the 2008 M_W 7.9 Wenchuan earthquake with rupture of geometric barriers in a cascading manner (Shen et al., 2009). In addition, Ren et al. (2022) and Yao et al. (2022) reported that the rupture length of the Maduo earthquake (~160 km), as well as that of some other strong earthquakes which have occurred around the BHB, such as the 1997 M_W 7.5 Manyi earthquake (185 km), the 2001 M_W 7.8 Kokoxili earthquake (420 km), and the 2010 M_W 6.9 Yushu earthquake (50–70 km), are all greater than the expected values for their magnitudes based on the commonly-used empirical relationships (Wells & Coppersmith, 1994).

The majority of moment release during the 2021 Maduo earthquake occurred above 10 km depth. Significant slip occurred in the central depth range of the seismogenic layer (1–10 km), which is similar to rupture patterns of a number of shallow strike-slip events, as demonstrated in Jin and Fialko (2021b). Besides, the spatial pattern of our slip distribution is generally complementary to aftershocks. Most of aftershocks were located in the depth range of 8–15 km (W. Wang, Fang, et al., 2021); dense aftershocks clustered below the hypocenter (Slip Void I in Figure 3a). Aftershocks were sparsely distributed to the west of the secondary splay (Slip Void II) where large coseismic slip occurred at shallow depths. The low aftershock densities may give a hint of a supershear rupture segment (e.g., Yue et al., 2022).

The relatively low values for shallow strike-slip movement estimated from our model are also in agreement with those measured from fieldwork (Z. Li et al., 2021; Pan et al., 2021; Ren et al., 2022) (Figure 4a), which favor a shallow slip deficit (SSD) (H. Chen et al., 2021; Hong et al., 2022; Jin & Fialko, 2021b; S. Wang, Song, et al., 2022; Yue et al., 2022; Zhao et al., 2021) (Figure 4b and Table 1). However, there are some noticeable differences in the magnitude of shallow slip and the amount of SSD among published studies. The general offsets from field mapping are 1–2 m and the maximum is ~3 m (Z. Li et al., 2021; Pan et al., 2021; Ren et al., 2022) (Figure 4a). Some studies (e.g., Hong et al., 2022; M. Wang, Wang, et al., 2021; Yue et al., 2022) resolved shallow slips systematically larger than field measurements. One possible explanation is that the slips in previous models were averaged over a relatively large patch size (3 km or larger). A smaller subfault size (e.g., 1 km) at shallow depth allows to resolve a finer-scale SSD. A moderate (50%) SSD was observed in our model. Jin and Fialko (2021b) reported a relatively lower level (30%) of SSD using a similar-scale patch size at the shallowest part, which is likely due to their application of a layered elastic half-space and a different regularization constraint (i.e., the first-order Tikhonov regularization). In addition, we note that precise comparison between predicted surface slip and the fieldwork result can be difficult. The soft sedimentary layer and abundant water sources make it challenging to measure offsets through geomorphological markers in the field. Field surveys only measured the near-field offsets while slip models depicted integrated dislocations over a subfault zone. The surface rupture can be more diffuse and complicated, for example, inelastic deformation which cannot be modeled using the elastic dislocation theory. This may also explain the discrepancies between inverted slips and field measurements, and the near-field residuals from geodetic inversion.

The geodetic moment of our model is 1.77×10^{20} Nm ($1.59–1.95 \times 10^{20}$ Nm within the 2-sigma uncertainty), corresponding to an $M_W \sim 7.43$ event. This is consistent with other geodetically derived moments but higher than the seismic moments reported by GCMT and USGS, which are in the range of $1.31–1.66 \times 10^{20}$ Nm (Table 1). Part of this difference ($\sim 0.3 \times 10^{20}$ Nm) is likely due to the effect of 5-day postseismic deformation included in the InSAR data.

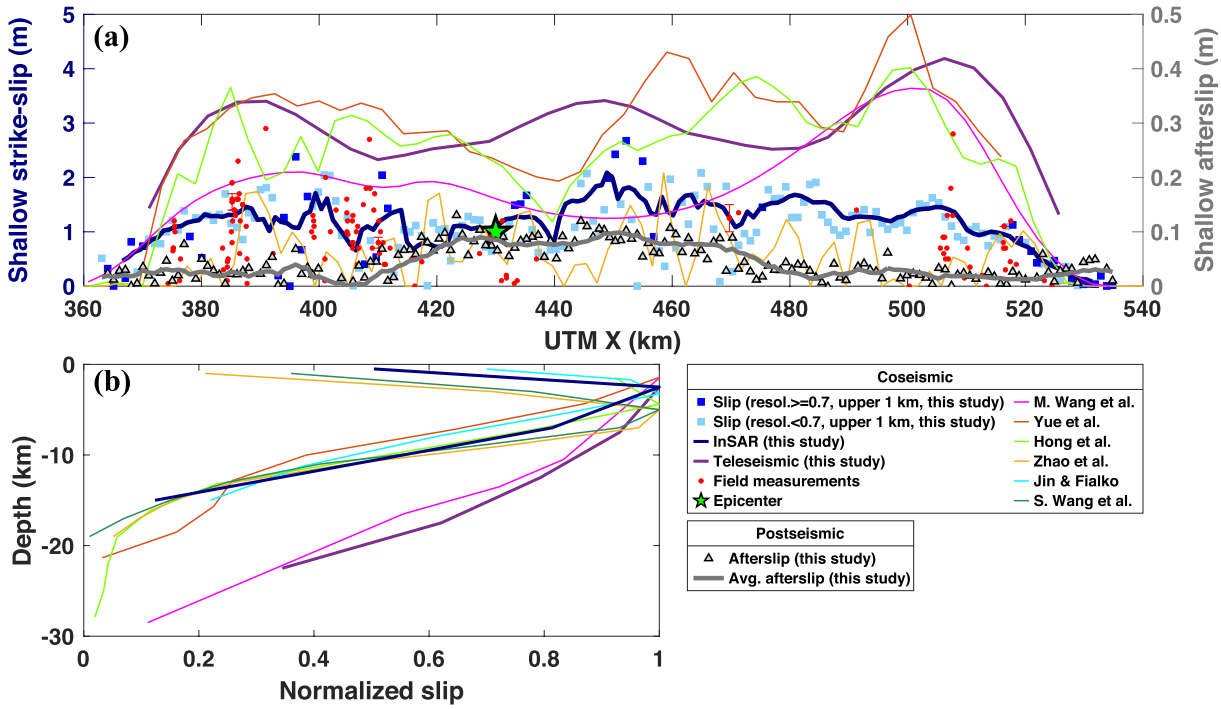

Figure 4. (a) Slip (dark-blue and light-blue squares) and afterslip (gray triangles) variations at shallow depth (0–1 km) along strike of the fault. Navy blue and gray lines are the along-strike moving average weighted by the associated standard deviation. Dark blue squares represent slips on patches with resolution ≥0.7. Red dots denote the coseismic offsets measured from field observations (Z. Li et al., 2021; Pan et al., 2021; Ren et al., 2022). Surface slip profiles from published models are shown in colored lines. (b) Along-strike averaged normalized coseismic slip as a function of depth for this study (InSAR and teleseismic) and published models.

Our resolution map (Figure S14 in Supporting Information S1) suggests that slip on most patches is robustly resolved, except in some shallow parts where InSAR observations experienced decorrelation in the near field. Our model recovers the InSAR data very well, with the root mean square (RMS) of residuals of ~4.5 cm (Figure 2 and Figure S4 in Supporting Information S1). The remaining residuals occur near the fault traces, which is likely due to complex (inelastic) deformation in the near field (Z. Li et al., 2021; Pan et al., 2021; Ren et al., 2022) that cannot be modeled based on elastic dislocation theory (Okada, 1985).

Existing modeled fault geometries and slip distributions are notably different among the published results (Table 1 and Figure 4). These dissimilarities are primarily attributable to the ill-posed nature of the slip inversion problem and different smoothing or regularization constraints applied (e.g., Gombert et al., 2018). One of the advances of our model is that we build a more realistic fault geometry designed from the combined tighter constraints from the SAR range offsets of the surface trace and the distribution of relocated aftershocks at depth (W. Wang, Fang, et al., 2021). To test whether the dips estimated by relocated aftershocks are reasonable constraints for geodetic inversion, we shifted the aftershock-derived dips by 5° systematically northward and southward. The slip distributions remained similar while the RMS of residuals increased by 8% and 13%, respectively (Figures S15 and S16 in Supporting Information S1). We note that the aftershock sequence relocation (W. Wang, Fang, et al., 2021) implies that there might be a secondary branch in the western end. However, this cannot be inferred from the InSAR data, although L. He, Feng, et al. (2021) suggest a blind segment which features relatively minor slip and no surface rupture. Therefore, we omit a secondary splay in the west and focus on the primary rupture. Another advantage of our slip model is that we apply von Karman regularization. As different fault geometries and regularization techniques could have important implications for interpreting slip distribution and modeling stress changes, our fault geometry configuration and regularization constraint allow us to better assess fault slip behavior and hence seismic hazard. Our model sheds light on the geometry- and lithology-related slip behavior (Section 4.2). Besides, we account for standard deviation of the slip model (Figure S17 in Supporting Information S1) in a Bayesian framework. The maximum standard deviation is ~0.3 m. Major uncertainties correlate with larger slip. The shallowest patches feature relatively smaller standard deviation.

Table 1
Compilation of Key Findings From Published Source Parameters (Bolded Results From This Study)

Data constraint	Dip (°)	Fault segments	Patch size (km^2)	Peak slip (m)	Depth (km)[a]	SSD (%)[b]	Moment ($\times 10^{20}$ Nm)	M_W	Source
Seismology	87	–	–	–	–	–	1.66	7.4	GCMT
Seismology/Sentinel-1 InSAR	76	1	3.5 × 3.5	~4	10	–	1.31	7.4	USGS
Seismology/Sentinel-1 InSAR	84	7	6 × 4	6.82	10	–	2.27	7.51	W. Wang, He, et al. (2022)
Seismology/Sentinel-1 InSAR	70/79/81[c]	3	5 × 3	~6	3–6	–	1.7	7.4	X. Zhang, Feng, et al. (2022)
Sentinel-1 InSAR	Variable	5	2 × 2	~6	5	Significant	–	7.38	Zhao et al. (2021)
Sentinel-1 InSAR	Variable	Non-planar	Triangular	~4.2	6–8	–	1.80	7.4	K. He, Wen, et al. (2021)
Sentinel-1 InSAR	83	2	2 × 2	~7.2	7	64	1.71	7.4	S. Wang, Song, et al. (2022)
Sentinel-1 InSAR	80	7	Variable	~6	3.2	30	–	7.46	Jin and Fialko (2021b)
Sentinel-1 InSAR	Variable	5	2 × 2	~5	4–7	Moderate	1.45	7.41	H. Chen et al. (2021)
Sentinel-1 InSAR	Variable	6	Triangular	5	6	–	1.58	7.43	L. He, Feng, et al. (2021)
Sentinel-1 InSAR	Variable	Non-planar	2 × 2	4.87	<10	–	–	7.5	Q. Zhang, Wu, et al. (2022)
Sentinel-1/ALOS-2 InSAR	90	Non-planar	Triangular	6	4–5	–	1.8	7.44	J. Liu et al. (2022)
GNSS	87	4	3 × 3	~3.6	1.5	–	1.82	7.4	M. Wang, Wang, et al. (2021)
GNSS/Sentinel-1 InSAR	Variable	6	2 × 2	~9.3	7	–	~1.5	7.39	Guo et al. (2021)
Sentinel-1/ALOS-2 InSAR/ GNSS	78/64[d]	Non-planar	3 × 3	4.07	4.4	10	1.65	7.42	Hong et al. (2022)
Sentinel-1/ALOS-2 InSAR/ GNSS	89/86/89[e]	3	Variable	4.1	<5	–	1.78	7.43	Q. Li, Wan, et al. (2022)
Sentinel-1 InSAR/Seismology/ high-rate GNSS	80	4	5 × 5	4.2	7.4	–	1.65	7.4	K. Chen et al. (2022)
Sentinel-1/ALOS-2 InSAR/ Seismology/GNSS	83	Non-planar	3.9 × 2.9	5	1.4	10[f]	1.43	7.37	Yue et al. (2022)
Sentinel-1 InSAR	**Variable**	**13**	**Variable**	**~7**	**2.5**	**50**	**1.77**	**7.43**	**This study**
Seismology	**90**	**Non-planar**	**5 × 5**	**~5**	**2.5**	–	**2.5**	**7.5**	**This study**

[a]Depth at which peak slip occurred. [b]Shallow slip deficit. [c]Dip of the western, central, and eastern segments, respectively. [d]Dip of the main and secondary rupture, respectively. [e]Dip of the western and central-eastern segments of the main fault, and dip of the secondary splay. [f]10% of Shallow slip deficit above the second row of asperity 2 in Yue et al. (2022).

3.2. Rupture Evolution

Our finite-fault rupture evolution model obtained from the teleseismic waveforms (Figure 5) reveals a bilateral rupture history, with a dominant eastward rupture, composed of three notable rupture episodes (Figure 6). For the first 11 s, the rupture initiated at the hypocenter, and then expanded to both east and west directions from the hypocenter at a speed of 3–5 km/s. The initial slip pulse ruptured mostly the shallow part of the model domain (<12.5 km depth). From 12 to 20 s, a second rupture pulse migrated primarily toward east from the hypocenter, rupturing from shallow to deep depth. During this rupture episode, the rupture appeared to be back-propagating (between 14 and 20 s), which is similar to what have been observed in some other earthquakes, such as the 2016 M_W 7.1 Romanche earthquake (Hicks et al., 2020), the 2019 M_W 8.0 Peru earthquake (Hu et al., 2021), and the 2020 Caribbean earthquake (Tadapansawut et al., 2021). And then a third rupture episode started from ~20 s, which ruptured the rest of the shallow part in a bilateral direction, at a speed of ~3 km/s. From 30 s onwards, relatively minor moments were released without any notable rupture episodes. The rupture finally ceased at 40 s. Our preferred rupture model can explain the observed teleseismic waveforms very well, with a 67% variance reduction (VR) of waveform fitting (Figure 5).

The total seismic moment release is 2.5×10^{20} Nm ($M_W \sim 7.5$) during the 2021 Maduo earthquake, which is larger than the reported seismic moment, for example, 1.7×10^{20} Nm for the GCMT solution (Dziewonski

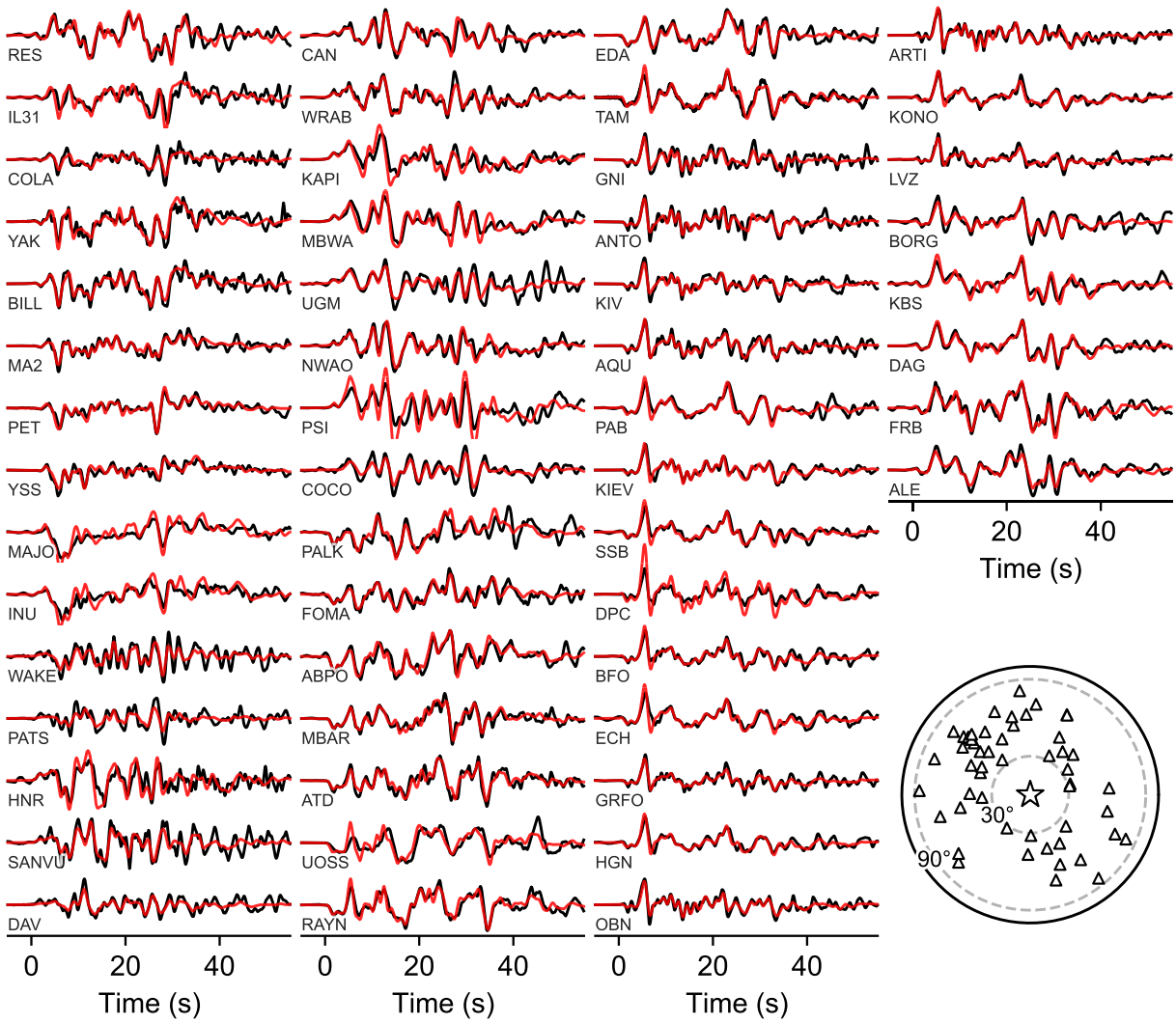

Figure 5. The observed (black) and synthetic (red) teleseismic waveforms for the finite-fault solution. The station code is shown in each panel. The bottom-right panel shows the station distribution.

et al., 1981; Ekström et al., 2012). This discrepancy is likely partly due to our selection of a wide enough model domain to capture all the possible rupture evolution (e.g., Tadapansawut et al., 2021). Also, our teleseismic modeling scheme allows fault geometry to change during the rupture propagation. In other words, we solve for variable moment-rate tensors for each sub-fault at each time step during the rupture. Thus, our inversion procedure can flexibly represent the moment release history, rather than assuming a fixed simplified (e.g., triangular) moment-rate function based on the point-source assumption adopted in other CMT solutions. If such a simple representation of moment release history may miss possible extra contributions from the source complexity, the resultant seismic moment from other CMT solutions would have been underestimated. In this study, we use seismology to focus on the rupture evolution of the 2021 Maduo earthquake, but not the absolute moment at a given fault location. Discrepancy of seismic moment with other means (e.g., CMT solutions, InSAR model) remains to be further studied by joint use of geodetic data, so that we may evaluate or match the final moment distribution to the one derived from geodetic data.

K. Chen et al. (2022) show a bilateral slip-pulse rupture at a sub-Rayleigh speed of 2.6–2.8 km/s from joint inversion of Sentinel-1 InSAR, high-rate GNSS and teleseismic waveforms. However, they assume in advance the allowed maximum rupture speed to be sub-Rayleigh (<3.6 km/s), precluding the possibility of supershear rupture. Their 4-segment fault geometry might be oversimplified and their fit to teleseismic waveforms is relatively poor (with 45% VR). In terms of our teleseismic finite-fault inversion, we select a wide enough model

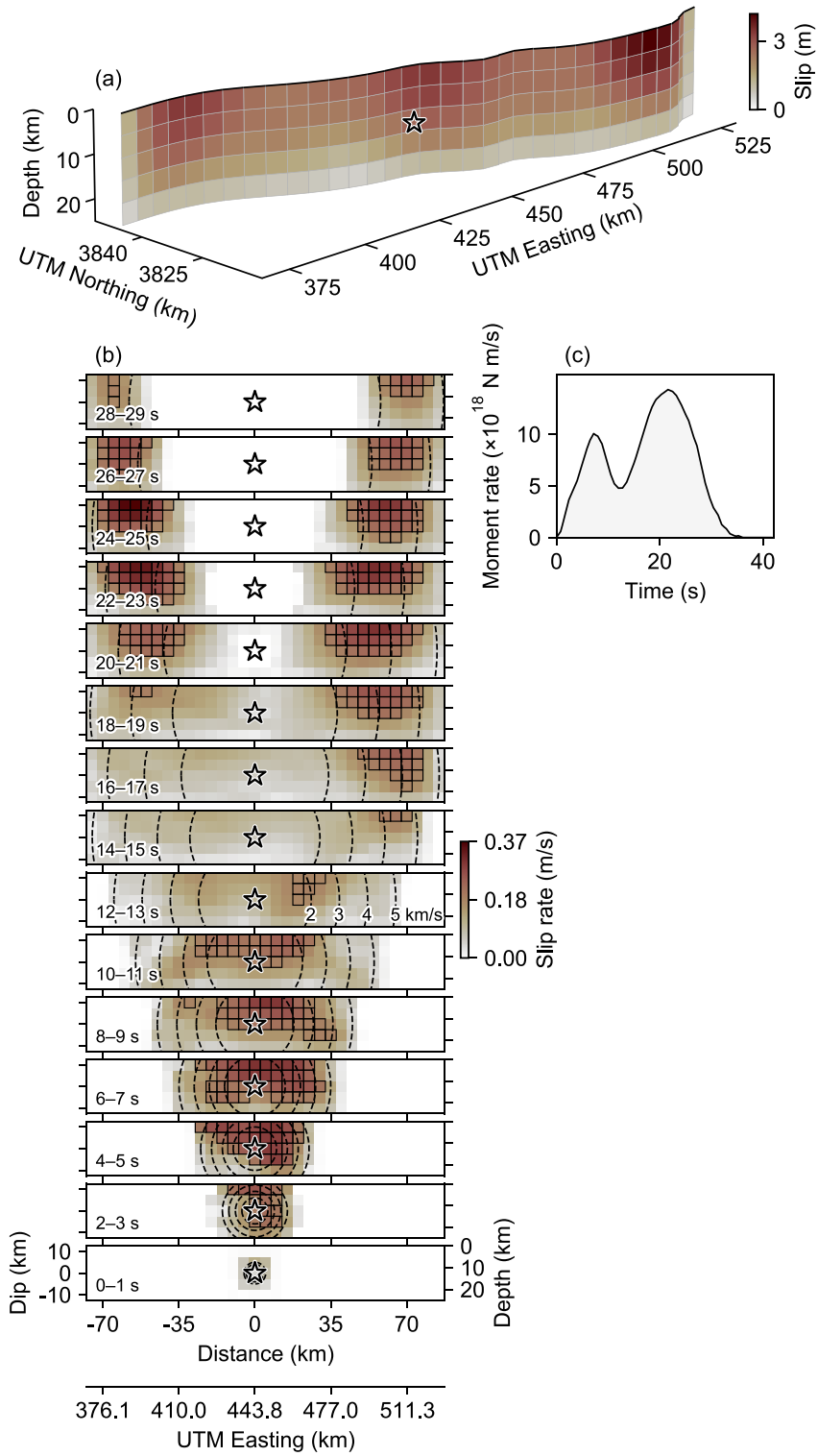

Figure 6. Rupture evolution derived from teleseismic waveforms. (a) Cumulative slip distribution. The star shows the hypocenter. (b) The cross sections of the spatial-temporal distribution of slip rate given in 1 s long windows. The black circles show the reference rupture speeds. Major slipping areas (>50% of the maximum slip rate) are outlined by the black cell boarders. (c) The moment-rate function.

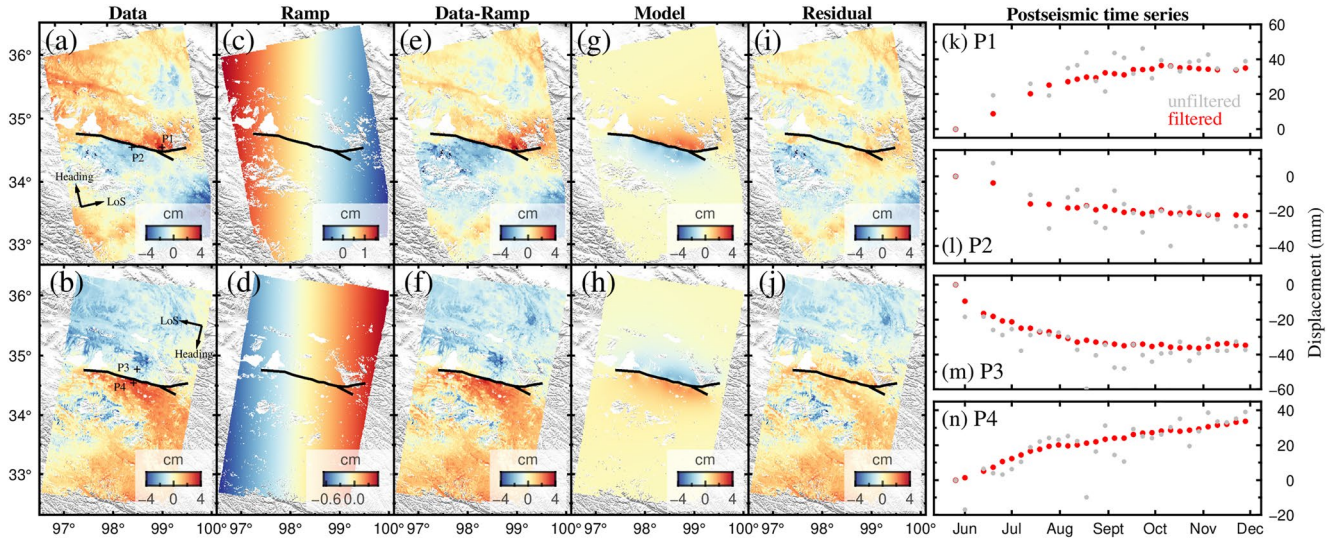

Figure 7. ~6-month (2021/05/26–2021/11/28) cumulative postseismic displacements (a, b), a best-fit ramp (c, d), removal of ramp (e, f), model fitting (g, h), and residuals (i, j). Positive value means displacement toward the satellite. (k–n) Postseismic displacement time series of selected pixels shown as black crosses in (a, b). Gray and red dots represent unfiltered and filtered results, respectively.

domain to consider all possible solutions. The apparent relatively fast rupture speed at an initial stage may be reflecting fast triggering of the initial rupture episode or supershear rupture propagation (e.g., Yue et al., 2022).

Our seismology solution shows good consistency with the slip model derived from the InSAR data. However, relatively large shallow slip was resolved from teleseismic data, which is partly caused by larger patch size at shallow depth. The teleseismically-derived peak slip was less than that from InSAR data. This is likely attributable to different inversion schemes and regularization constraints. A slightly higher slip (~2.8 m) around the hypocenter was found teleseismically, compared with the InSAR-derived result (~2 m). Part of this difference is likely due to the temporal smoothing effects. The strength of smoothing is objectively determined on the basis of ABIC, which is primarily controlled by information included in the data (e.g., Fukahata & Wright, 2008). Because the teleseismic finite-fault inversion resolves the timing and location of the slip which are only relative to the presumed hypocenter (i.e., initial rupture point, Section 2.5.3), and the spatial resolution of the teleseismic data is limited compared to that of the InSAR data, a comparison of the absolute location of the slip between the teleseismic solution and the InSAR results cannot be rigorously made. In this study, we use teleseismic data as an independent measurement to get a sense of spatiotemporal evolution of rupture during the Maduo earthquake. Our teleseismic inversion algorithm is currently not designed to incorporate data other than teleseismic *P* waveforms. We leave the joint inversion of geodetic and seismic data for future work.

3.3. Early Afterslip Models

The cumulative postseismic displacements over each time period and model fitting are shown in Figure 7 and Figures S18–S22. Our models of early afterslip over each time interval reveal several key features (Figures 3b, 3c and 3d and Figure S23 in Supporting Information S1). Coseismic slip deficit is taken up by both shallow and deep afterslip occurring in the first ~6 months following this earthquake (Figure 3). Around 0.1 m of afterslip occurred at shallow depths while 0.2–0.4 m of afterslip occurred below the seismogenic zone. Shallow (<4 km) and deep (>10 km) depths show different afterslip evolutions with time (Figures 3c and 3d); shallow afterslip grows linearly with time while deep afterslip grows logarithmically. This may reflect spatial variations in frictional properties of the fault, as evidenced by lithological contrasts (Figure 8) (see Section 4.2). There is lack of afterslip in the depth range of 4–10 km, consistent with where we might expect velocity weakening material. We also note that relatively minor (30% below average) coseismic slip occurred around the epicenter where major shallow afterslip occurred linearly with time (Figure 3d).

Postseismic moment release during the first ~6 months (2021/05/26–2021/11/28) is 2.54×10^{19} Nm ($2.25–2.83 \times 10^{19}$ Nm within the 2-sigma uncertainty), equivalent to an $M_W \sim 6.91$ event. We analyze the

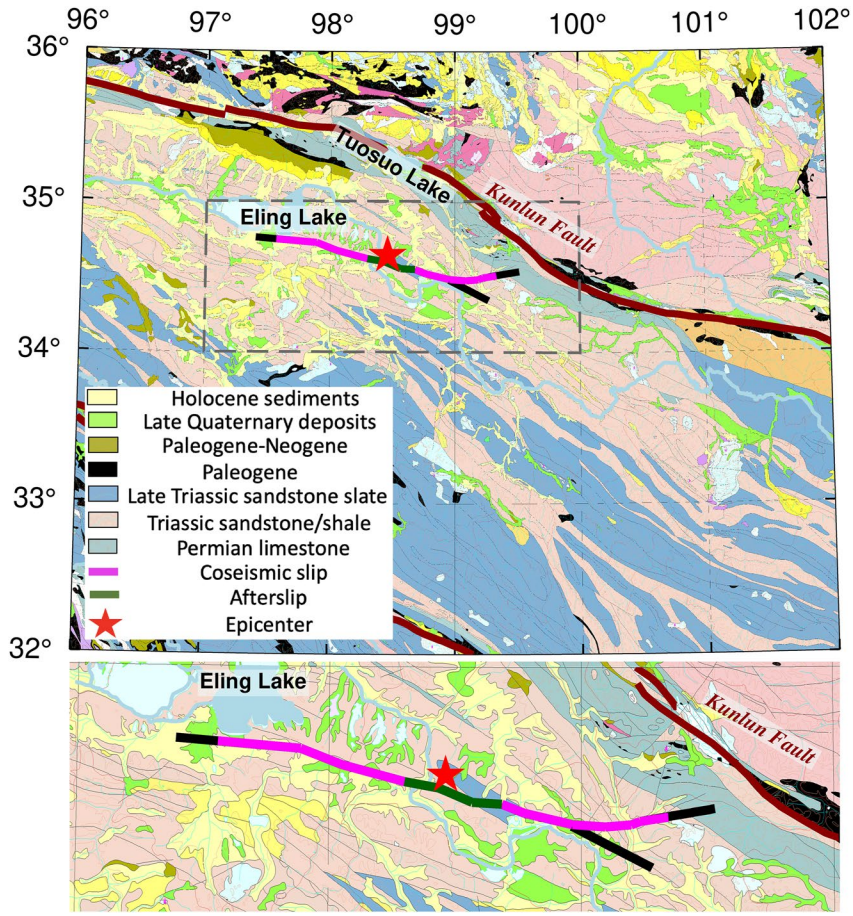

Figure 8. Distribution of lithological units, complied by Pang et al. (2017a); Pang et al. (2017b) (available at http://dcc.ngac.org.cn//geologicalData/details/doi/10.23650/data.H.2017.NGA105570.T1.64.1). Red star marks the epicenter of the 2021 Maduo earthquake. Black lines represent surface rupture traces. Magenta and green lines show the predominant coseismic slip (≥1 m) and major afterslip (≥0.1 m) segments at shallow depths, respectively. Bottom panel is a zoomed view around the rupture zone delimited by the dashed rectangle in the top panel.

temporal variations of postseismic moment release in the first ~6 months and solve for the moment occurring in the first 5 days (2021/05/21–2021/05/26) postseismically by fitting a logarithmic model back to the date of the earthquake (Figure S24 in Supporting Information S1). The largest part of the postseismic moment has been released by the deep afterslip in the depth interval of 10–20 km over those ~6 months. We estimate the moment release between the date of the earthquake and the first post-earthquake SAR acquisition to be 4.38×10^{18} Nm ($3.61–8.08 \times 10^{18}$ Nm within the 95% confidence intervals). An exponential decay function is also used to represent the postseismic moment relaxation, which gives the first 5-day moment release of 1.27×10^{18} Nm ($0.89–1.49 \times 10^{18}$ Nm within 95% CI, Figure S24c in Supporting Information S1). Both logarithmic and exponential relaxation forms provide a reasonable fit to the postseismic moment time series. However, regardless of the functional forms, the predicted moment released during the first 5 days postseismically can only partly explain the difference between the geodetically- and seismically-derived coseismic moments (i.e., $\sim 3 \times 10^{19}$ Nm); the difference between the moments likely arises from other systematic errors, such as those resulting from differences in elastic structure and fault geometry.

To test if the deep afterslip (i.e., within 10–20 km depth range) is required by the data, we invert for an afterslip model with the deep patches excluded. The result indicates the deep afterslip is necessary to explain the postseismic observations, especially the mid-field (10–50 km) deformation (Figure S25 in Supporting Information S1). The RMS of residuals (~1.5 cm) increased by 50% compared to that with the deep patches included (~1 cm). We therefore suggest that deformation occurring at 10–20 km depth is required in the near-to-mid field of the rupture.

3.4. Interseismic LOS Velocity and Strain Rate Fields

Figure 9 shows the east-west velocities and shear strain rate fields over a ~700 km by ~400 km region centered on the Jiangcuo Fault. No GNSS velocities were reported by M. Wang and Shen (2020) within the 20 km-wide 400 km-long InSAR profile, but good agreement is observed between GNSS V_E within a 200 km-wide profile and the InSAR V_E, both filtered and unfiltered (Figures 9a and 9b). We observe shear strain localized not only on the KF, but also on the Bayan Har Shan Main Peak Fault, as confirmed by the steps in the unfiltered and filtered east-west velocity profiles, that is, ~2 mm/yr contrast across the Bayan Har Shan Main Peak Fault and ~5 mm/yr change across the KF (Figures 9a and 9b).

The strain rate we calculated is derived from four horizontal velocity gradients (Figure S13 in Supporting Information S1, Ou et al., 2022). It is clear that the velocity gradients of interpolated GNSS velocities are of lower value and of longer wavelength than that derived from median-filtered InSAR as expected from the fewer GNSS stations and the resultant interpolation. The resolution of the InSAR-derived velocity gradients hence strain rate comes from the high-density measurements which, when coupled with the median filter that preserves the shape while quenching the noise, highlights strain localization much more effectively. The width of the strain feature on the map view may reflect the actual extent of the strain rate peak, which mathematically corresponds to the distance over which the velocity change occurs. The peak value of 111 nanostrain/yr derived for this region agrees with another InSAR-derived result (Zhao et al., 2021); both are significantly larger than the GNSS strain rate (20–30 nonastrain/yr, M. Wang & Shen, 2020). This peak value corresponds to the point of the steepest velocity gradient, which is where the KF sits. Ou et al. (2022) suggest that InSAR-derived strain rate field is consistent with the GNSS-based result (M. Wang & Shen, 2020) in the long wavelength, with an average second invariant misfit value of 10 nanostrain/yr. InSAR-based strain rates are better localized and more reflective of the actual distance over which velocity change occurs as compared to the lower-resolution GNSS-based strain rate values that we are used to seeing.

The velocity gradient across the Jiangcuo Fault is only 1–2 mm/yr over a distance of <100 km which gives rise to 20–40 nanostrain/yr of shear strain rate between 2014 and 2021. The surface rupture of the 2021 Maduo earthquake coincides with a small strain rate peak on the profile. However, due to the ~10 nanostrain/yr of uncertainties in the strain rate field (Ou et al., 2022), this strain rate peak is almost indistinguishable from other small peaks away from the fault (Figure 9c).

The apparent southward shift of the strain peak relative to the KF (Figure 9c) is likely the result of the low InSAR pixel density to the south of the KF relative to that to the north. The near north-south trending shear feature to the west of the profile is a result of the apparent east velocity difference on both sides of the area of decorrelated InSAR V_E in Figure 9a. The location, shape and degree of localization of this strain feature is poorly constrained due to the low pixel density of the InSAR V_E.

The dilatation rate shows contraction near the fault bends along the KF and the Bayan Har Shan Main Peak Fault (Figure S13f in Supporting Information S1). Apparent dilatation occurs at the western tip of the Maduo rupture, corresponding to the transtensional fault bend (Zhao et al., 2021) and consistent with the east-west collapse of the high plateau suggested by previous studies (Coleman & Hodges, 1995; Molnar & Tapponnier, 1978).

4. Discussion

4.1. Low Slip Rate Faults in "Block" Interiors

Localized deformation around locked faults appears to be commonly observed and has been widely reported (Daout et al., 2018; Jolivet et al., 2015; H. Wang et al., 2009; Wright et al., 2013; Weiss et al., 2020). More tectonically active faults produce larger geodetic signals and attract more attention for research. Geodetic block models have tended to focus on only the fastest moving faults, while slow moving faults, where the geodetic signal-to-noise ratio can be low, are often neglected. Although major block boundaries are usually considered to be the major source of seismic hazard, there are many large earthquakes which have not occurred on the major pre-identified block boundaries. For example, even in well-mapped and understood regions like California, earthquakes such as the 1992 M_W 7.3 Landers earthquake (Massonnet et al., 1993), the 1999 M_W 7.1 Hector Mine earthquake (Gomberg et al., 2001), and the 2019 Ridgecrest earthquake sequence (Ross et al., 2019), have all occurred away from the major mapped structures of the San Andreas fault system. These earthquakes hit

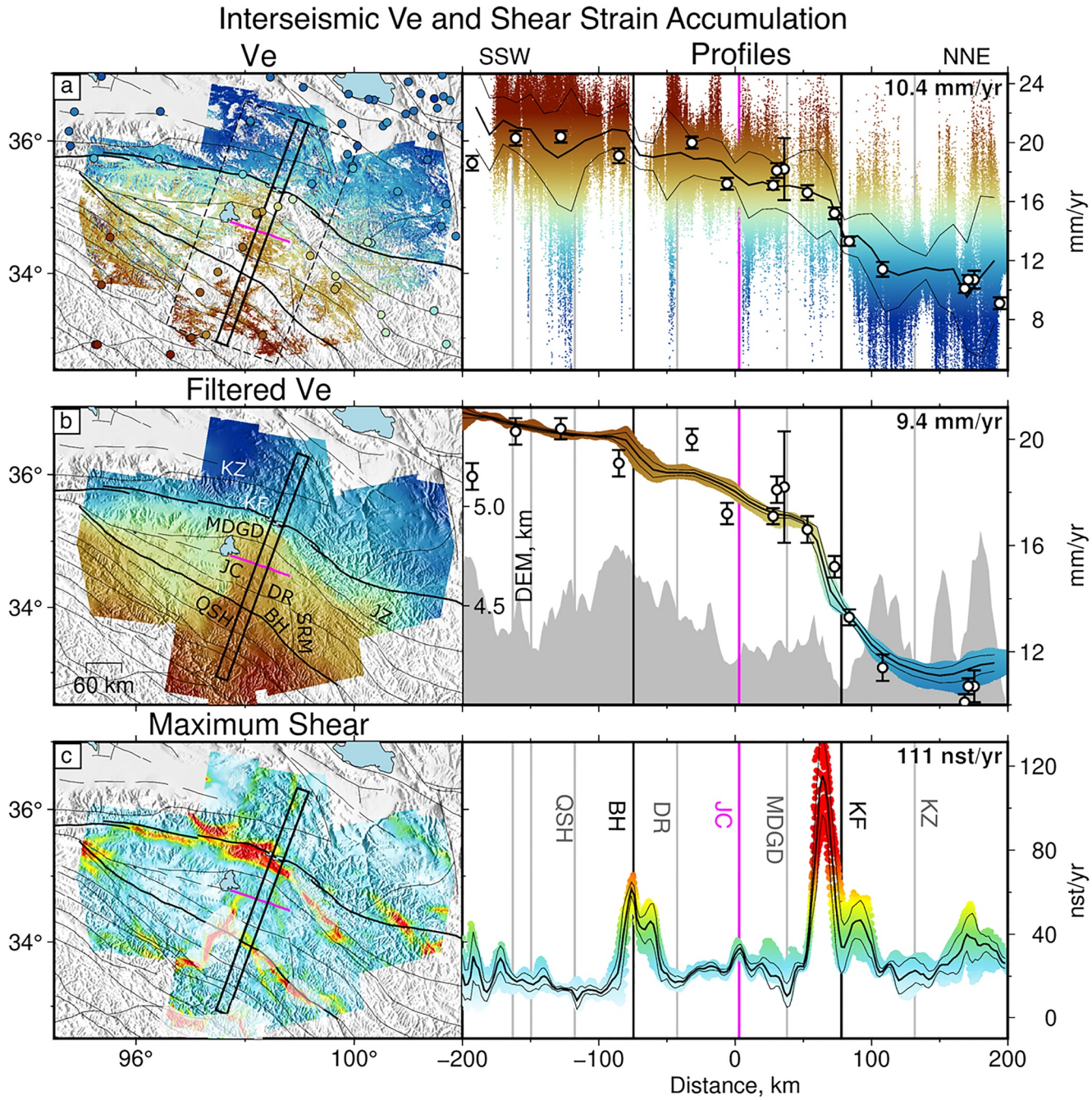

Figure 9. Map views and profile views of the 100 m-resolution east velocities (a), east velocities median filtered by a 60 km-diameter circular filter window and sampled at 1 km pixel spacing (b), and maximum shear strain rates with the same 1 km sampling spacing (c). GNSS V_E from M. Wang and Shen (2020) are plotted as dots in (a); those within a 200 km-wide profile (dashed line) centered around the 20 km-wide InSAR profile (solid line) are plotted with error bars on top of the InSAR profiles. Transparent overlay on top of the strain rate map (c) represents the areas of low pixel density of V_E (a). Thick and thin black lines within the profiles show medians and standard deviations within 5 km (a, b) and 1 km (c) distance bins. Magenta vertical lines on profiles and thick magenta lines on maps show the location of the seismogenic fault of the 2021 Maduo earthquake. Black vertical lines on profiles and thick black lines on maps show the locations of the KF and the Bayan Har Shan Main Peak Fault with observed interseismic shear strain accumulation. Gray lines show other faults mapped by Q. Deng et al. (2003). A topographic profile is shown in (b). Labels on the top-right corners of the profile panels show the difference between the mean values on both ends of the east velocity profiles, and the maximum mean value along the maximum shear strain rate profile which corresponds in space to the steepest gradient along the filtered V_E profile in (b). Abbreviations of fault names: KZ = Kunzhong Fault, KF = Kunlun Fault, MDGD = Maduo-Gande Fault, JC = Jiangcuo Fault, DR = Dari Fault, BH = Bayan Har Shan Main Peak Fault, QSH = Qingshuihe Fault, JZ = Jiuzhi Fault, SRM = Sangrima Fault.

the Eastern California Shear Zone, a broad zone of distributed shear which was pre-recognized based on fault mapping, structural analyses, and ground-based geodesy (Dokka & Travis, 1990a, 1990b).

Slow slip-rate faults tend to be characterized by long recurrence intervals. However, slow slip rates do not necessarily imply limited earthquake potential (Anderson et al., 1996; Galli & Peronace, 2015; K. Li et al., 2019; Shen et al., 2009; Radiguet et al., 2009; K. Wang, Zhu, et al., 2021). For instance, a low slip rate (0.08–2 mm/yr derived geologically) fault hosted the 1992 M_W 7.3 Landers earthquake (Anderson et al., 1996). The Landers earthquake sequence showed a mechanism for transferring the plate boundary motion into the block interior (i.e., the Eastern California Shear Zone) (Hauksson et al., 1993). The Tanlu Fault, with a dextral slip rate of 0.7 mm/yr since the late Pleistocene (K. Li et al., 2019), generated the 1668 M 8.5 Tancheng (eastern China) earthquake. Another typical example is the devastating 2008 M_W 7.9 Wenchuan earthquake in China, despite low (<3 mm/yr) deformation rate across the Longmen Shan fault zone (Z. Chen et al., 2000; Shen et al., 2005; P.-Z. Zhang, Shen, et al., 2004). Similarly, the Jiangcuo Fault features a low slip rate of 1.2 ± 0.8 mm/yr and a long earthquake recurrence interval of up to 1,100–5,500 years (Y. Zhu, Diao, et al., 2021). The occurrence of the 2021 M_W 7.4 Maduo earthquake further emphasizes that the seismic hazard posed by low interseismic strain accumulation along historically quiescent faults cannot be ignored.

Earthquakes may behave differently because of the maturity of the causative faults. Immature fault systems tend to be more geometrically complex and produce shorter, slower, yet more energetic ruptures (Manighetti et al., 2007, 2021; Perrin et al., 2016; Radiguet et al., 2009), for example, during the 1992 M_W 7.3 Landers earthquake (Peyrat et al., 2001; Sieh et al., 1993), the 1999 M_W 7.1 Hector Mine earthquake (Ji et al., 2002), the 2010 M_W 7.2 El Mayor-Cucapah earthquake (Wei et al., 2011), the 2016 M_W 7.8 Kaikoura earthquake (Cesca et al., 2017; Hamling et al., 2017), and the 2019 Ridgecrest earthquake sequence (Goldberg et al., 2020). By contrast, earthquakes with high rupture velocities are typically related to well-developed faults (Perrin et al., 2016), such as the 2001 M_W 7.8 Kokoxili earthquake and the 2002 M_W 7.9 Denali earthquake (Ozacar & Beck, 2004; Walker & Shearer, 2009) as well as the 2018 M_W 7.5 Palu earthquake (Bao et al., 2019; Socquet et al., 2019), all of which have occurred on major block boundaries. While mature faults appear to be geometrically simpler, shear zones in the initial stage of faulting have generally more complex geometries with fault segmentations and variable disorganized orientations (Crider & Peacock, 2004); as faults grow and develop through time, the fault segments tend to localize deformation and evolve from being hardly linked to fully linked; new step-overs may be created with the pre-existing ones smoothed out, leading to a more continuous and through-going fault trace with lower strength and lower fracture energy as the fault becomes more mature (Ben-Zion & Sammis, 2003; Manighetti et al., 2007, 2021; Wesnousky, 1988). These facilitate hosting strong earthquakes at fast speed (Manighetti et al., 2007; Perrin et al., 2016).

The maturity of the Jiangcuo Fault is still unclear. C. Li, Li, et al. (2022) and Zhao et al. (2022) suggest an immature seismogenic fault based on large off-fault deformation during the Maduo earthquake. Given the cumulative fault offset of 4–5 km (C. Li, Li, et al., 2022) and the geological rate of ~0.55 mm/yr (Pan et al., 2022), we infer that the Jiangcuo Fault possibly initiated at 7.3–9.1 Ma. Besides, the overall geometric expression of the Jiangcuo Fault geologically mapped by Q. Deng et al. (2003) is rather simple and straight, despite some local bends revealed by the SAR imagery. The fault trace adopted in our model is fully connected constrained by the SAR range offsets. The 2021 Maduo earthquake ruptured the surface and major slip occurred at shallow depths above 10–15 km, implying a relatively thin velocity-weakening brittle layer. Its relatively old age of initiation and overall geometrical simplicity, combined with the presence of major earthquakes lead us to infer that the Jiangcuo Fault is probably a well-developed fault capable of hosting large-magnitude earthquakes, and that the associated seismic hazard was ignored due to its low slip rate. Observations of potential supershear rupture speeds, as reported by Q. Li, Wan, et al. (2022), W. Wang, He, et al. (2022), Yue et al. (2022), and X. Zhang, Feng, et al. (2022), would support the suggestion that this is indeed a well-developed, structurally-mature fault, with fairly low slip-to-length ratio of the rupture ($\alpha = 5–10 \times 10^{-5}$) (e.g., Manighetti et al., 2007).

4.2. Lithological Controls on Slip and Afterslip

The mode of fault slip, ranging from aseismic slip, slow slip events, tremor, to earthquakes, has been linked with a fault's frictional properties (e.g., C. Marone, 1998; Scholz, 2019). Velocity-strengthening regions can arrest coseismic slip and host afterslip (e.g., Avouac, 2015; Boatwright & Cocco, 1996; Chlieh et al., 2007; Jolivet et al., 2013; Liu-Zeng et al., 2020; C. Marone, 1998; Scholz, 1998, 2019). We observed a moderate

SSD (50%) in the 2021 Maduo earthquake, which is likely governed by the frictional resistance of a shallow velocity-strengthening layer (C. Marone, 1998). In the first ~6 months following the 2021 Maduo earthquake, coseismic slip deficit is partly taken up by afterslip. The different temporal evolution patterns of afterslip in shallow and deep regions are likely caused by heterogeneity in fault friction, which are at least in part governed by lithological strength contrasts (Figure 8) and depth-dependent differences in temperature, pressure, pore pressure, etc (e.g., M. Xu et al., 2011). The different temporal-varying behavior of afterslip at different locations on the fault is similar to what has been observed in the 2014 Napa earthquake (Floyd et al., 2016).

We note that there is a spatial correlation between the lithology and slip type during and following the Maduo earthquake (Figure 8). Besides the possible relationship between geometrical barriers and the multi-peak coseismic slip pattern as discussed in Section 3.1, along-strike variations in slip may also be associated with laterally-varying lithological units. The Triassic sandstone/shale unit is widely distributed within the Bayan Har terrane. The predominant coseismic slip (≥1 m) regions generally occurred adjacent to Holocene/late Quaternary fluvial sediments. The slip on the southern branch of the eastern horsetail splays was insignificant compared with that on the northern branch, in spite of similar distribution of deposits. The northern branch was marked by tensional cracks, whereas the southern branch involved prominent compressional pressure ridges (mole tracks), some of which were in permafrost (Pan et al., 2022). Surface rupture expressions became discontinuous or missing and were characterized by liquefaction of sandstone around the epicenter (Pan et al., 2021) where we found major shallow afterslip (≥0.1 m) was concentrated. Shallow afterslip evolves linearly with a slightly different linear rate over short distances; afterslip rate is ~0.15 mm/day in late Triassic sandstone slate compared to ~0.27 mm/day in Triassic sandstone/shale (Figures 3d and 8). The correlation between lithology and spatiotemporal variability of slip modes suggests that lithology is exerting a control on the frictional properties of the fault, which may be related to heterogeneous mineral composition or pore/fluid pressure (Floyd et al., 2016; Thomas, Avouac, Gratier, & Lee, 2014; Weislogel, 2008). Sandstone is usually porous to allow the percolation of water and other fluids, which appears to be under high fluid pressure, impeding coseismic slip but hosting postseismic afterslip. Fluvial sediments are less permeable which we might expect velocity-weakening material facilitating earthquake slip. It is noted that there is an overlap between coseismic slip and postseismic afterslip (i.e., polygons C and D in Figure 3). This phenomenon has also been observed during the 2010 M_W 8.8 Maule earthquake (Bedford et al., 2013). This might be due to transient change of rate-and-state frictional properties from velocity weakening to velocity strengthening induced by shearing, similar to the frictional behavior of the Longitudinal Valley Fault (Thomas et al., 2017). On the other hand, as the 2021 Maduo earthquake occurred at the electrical boundary zone (Zhan et al., 2021), with resistivity contrasts likely reflecting different degrees of hydration above and below the hypocenter (at ~10 km depth), this may also contribute to different temporal evolutions of afterslip at shallow and deep depths. In addition, we note that unmodelled atmospheric delays in InSAR data might cause an apparent linear temporal evolution of afterslip/creep (e.g., Z. Li et al., 2009; MacQueen et al., 2020; Yu et al., 2020).

We have known for a long time that earthquakes result from frictional instability and many earthquake phenomena (including seismogenic rupture as well as pre- and postseismic phenomena, stress transfer processes, earthquake triggering, slow-slip phenomena, etc.) appear to be well explained by the rate and state friction law (Peng & Gomberg, 2010; Scholz, 1998; Steacy et al., 2005; R. S. Stein et al., 1997). The observed heterogeneity in behavior of the coseismic slip and postseismic afterslip during and after the 2021 Maduo earthquake may indicate spatially-varying constitutive parameters of the rate-and-state friction law, comparable to the spatial variations of rate-and-state frictional properties of the Longitudinal Valley Fault (Thomas et al., 2017). We suggest that short-scale variability of frictional properties, which are possibly associated with local lithological contrasts, should affect mechanical/dynamic modeling, fault slip behavior assessment and associated seismic hazard analyses (e.g., Pajang et al., 2021; Thomas et al., 2017).

4.3. Implications for Seismic Hazard

The 2021 Maduo earthquake is another significant event that happened on a slowly-slipping fault, analogous to the 2008 M_W 7.9 Wenchuan earthquake (P.-Z. Zhang, 2013a), highlighting the distributed nature of seismic hazard in tectonically active continental interior regions and the importance of slow-slipping faults in block interiors for seismic hazard analysis. As earthquake recurrence intervals are much longer than observational periods, a question remains how to interpret decadal measurements of "interseismic" deformation in terms of long-term

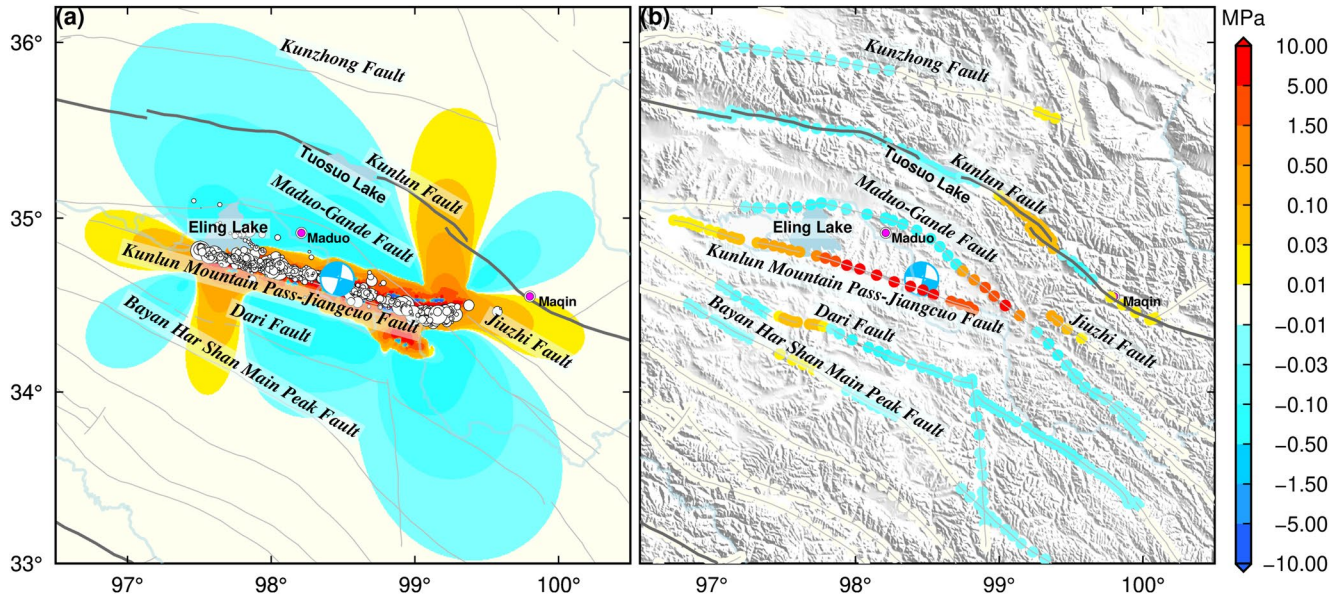

Figure 10. Coulomb Failure Stress change (ΔCFS) caused by the 2021 Maduo earthquake, (a) in the epicentral region and (b) on neighboring faults, calculated at a depth of 10 km where most aftershocks clustered. Relocated aftershocks are shown as white dots in (a). Beach ball represents the Maduo earthquake.

hazard. Geodetically-derived slip rates of major faults show, in general, agreement with geologic rates (W. Wang, Qiao, & Ding, 2021; Zheng et al., 2017), indicating that strain rates are basically steady through most of the earthquake cycle (Elliott et al., 2016) and that short-term geodetic observations can directly make contributions to long-term earthquake hazard assessment (Hussain et al., 2018; Wright, 2016). However, it is challenging to directly determine slip rates geodetically for faults with 1–2 mm/yr of slip or less (e.g., Calais & Stein, 2009; Newman et al., 1999; Smalley et al., 2005; S. Stein, 2007; Watson et al., 2022).

To assess the seismic hazard after the Maduo earthquake, we use the PSGRN/PSCMP code (R. Wang et al., 2006) to calculate the Coulomb Failure Stress change (ΔCFS) in surrounding area and on neighboring faults based on our preferred coseismic slip model shown in Section 3.1. We use a friction coefficient of 0.4 as different friction coefficients have little effect on the spatial pattern of ΔCFS (Guo et al., 2021; L. He, Feng, et al., 2021; Hong et al., 2022; Xiong et al., 2010). The crustal rheological structure consists of three layers: a 25 km thick elastic upper crust, a viscous Burgers-body lower crust with a thickness of 33 km, and a viscous Maxwell-body upper mantle; the transient and steady-state viscosities of the Burgers body are 4.0×10^{17} and 6.3×10^{18} Pa s, respectively; the viscosity of the Maxwell body is 1.0×10^{20} Pa s (full details in Hong et al., 2022). Our ΔCFS shows a similar pattern as published results (Guo et al., 2021; K. He, Wen, et al., 2021; Hong et al., 2022). We note that the 2021 Maduo earthquake caused positive stress changes of larger than 0.01 MPa on 2 segments of the KF: east of the Tuosuo Lake segment, and the Maqin segment which has drawn extensive concern of high seismic risk due to few historical earthquakes in the past ~1,000 years in this seismic gap (X. Wen et al., 2007; Xiong et al., 2010; L. Zhu, Ji, & Liu, 2021); besides, the western Jiuzhi Fault as well as part of the Dari Fault and the Bayan Har Shan Main Peak Fault in the west have experienced comparable increased ΔCFS (Figure 10). The Jiangcuo Fault could be considered as a southern splay of the KF and might be connected to the Kunlun Mountain Pass Fault in the west (Ha et al., 2022; Pan et al., 2021; M. Wang, Shen, et al., 2021), which ruptured during the 2001 M_W 7.8 Kokoxili earthquake (Ozacar & Beck, 2004; Walker & Shearer, 2009). The 2021 Maduo earthquake was likely brought closer to failure by the 2001 M_W 7.8 Kokoxili earthquake (Dong et al., 2022). The unbroken segment between the 2001 Kokoxili and 2021 Maduo ruptures should be of concern for elevated seismic hazard (Ha et al., 2022), especially the westward extension of the Jiangcuo Fault where a positive stress change was caused by the Maduo earthquake (Figure 10).

From the shear strain rate field (Figure 9c), we observe strain concentration on the KF and the Bayan Har Shan Main Peak Fault. It is worth noting that the Bayan Har Shan Main Peak Fault is in the interior of the commonly referenced BHB; the BHB is deforming internally. This echoes a similar observation made by Ou et al. (2022) where an unmapped structure is accommodating shortening near the eastern termination of the Haiyuan Fault

within the Longzhong Block, which was also thought to be rigid. As such, high-resolution strain rate fields derived from InSAR velocities are helping us better characterize the nature of continental deformation; as the observations get denser, it is clear that the deformation cannot be described by the motion of a few large blocks alone. Although significant strain is observed on many faults that bound larger blocks, additional deformation occurs within these larger blocks causing events such as the Maduo earthquake. One solution to capture this would be to build models with more, smaller blocks. However, if there are multiple faults with low strain rates, deformation may be better described as distributed strain within deformable blocks (e.g., Q. Chen et al., 2004; Loveless & Meade, 2011).

Distributed deformation within blocks is likely controlled in part by earthquakes with long recurrence intervals (Y. Zhu et al., 2020). The KF constitutes the northern boundary of the BHB and the Ganzi-Yushu-Xianshuihe Fault defines the southern boundary (Figure 1). Both play an important role in accommodating the eastward extrusion of the Plateau. The slip rate of the KF decreases gradually from the Tuosuo Lake segment toward the eastern end (Diao et al., 2019) while the shear motion increases along the Ganzi-Yushu-Xianshuihe Fault (Yue et al., 2022), suggesting a possible tectonic role of the BHB in transmitting shear motion and strain partitioning through a series of sub-parallel secondary faults in the interior (e.g., the Jiangcuo Fault, the Jiuzhi Fault, the Dari Fault, the Bayan Har Shan Main Peak Fault, etc.). The deformation along the KF may represent a diffuse tectonic block boundary, which accommodates differential motion between the BHB and the Qaidam Block in the north. The deformation in the BHB is characterized by east-west compression and north-south extension, accommodated by strike-slip faulting in the upper crust and distributed ductile shear and vertical thickening in the lower crust (M. Wang, Shen, et al., 2021). The diffuse deformation is indicated by the low-velocity zone in the mid-to-lower crust (H. Li, Shen, et al., 2014), high heat flow (Zhao et al., 2021), and high conductivity (Zhan et al., 2021), which may explain the relatively low strain localization along the Jiangcuo Fault.

Many seismic hazard models allow for background seismicity that can happen anywhere as well as seismicity associated with individual faults. Current probabilistic seismic hazard models are usually built on the basis of fault slip rates and dimensions (e.g., Rong et al., 2020). Some modelers separate on-fault and off-fault earthquakes before constructing seismicity models. Smaller ($M_W < 6.5$) earthquakes are being distributed within a seismic source zone; larger earthquakes are put onto active faults and into the zone as background seismicity. However, the hazard of all structures (known and unknown) should be considered in a consistent way. The seismogenic fault (i.e., the Jiangcuo Fault) of the 2021 Maduo earthquake was not included in hazard models due to its low slip rate. Our observations support the use of geodesy to improve hazard models, and the inclusion of large earthquakes on slow slipping faults. We have entered an era of geodetic big data as more and more SAR satellite data are being acquired with short revisit periods. The velocity and strain rate fields can be updated on a regular basis (e.g., annually or semi-annually) and therefore we will be able to investigate the temporal variations of strain accumulation rate. On the other hand, with data sets covering longer periods of observation and radar instruments using longer wavelengths for improved coherence (e.g., NISAR), illuminating low strain-rate shear away from major faults with InSAR is a foreseeable future.

5. Conclusions

In this study, we combine Sentinel-1 interferograms, SAR range offset maps, and relocated aftershocks to refine the fault geometry and slip distribution for the 2021 Maduo earthquake. We also reveal the rupture history based on an independent inversion of teleseismic data. By analyzing time series of postseismic deformation occurring in the first ~6 months following the Maduo earthquake, we explore the time-dependent afterslip behavior. We further assess the seismic hazard by characterizing the preceding interseismic strain accumulation and evaluating the stress loading caused by the Maduo rupture. We find that:

1. The 2021 Maduo earthquake occurred on an intrablock slow-slipping fault with relatively low interseismic strain localization (20–40 nanostrain/yr).
2. A bilateral rupture evolution which involved three notable episodes was resolved teleseismically.
3. A moderate (50%) SSD was observed based on our preferred self-similar slip model; slip maxima coincides with fault bends.
4. The coseismic slip deficit is taken up by both shallow and deep afterslip during the first ~6 months following the earthquake. Afterslip evolves linearly with time in the upper 4 km depth but evolves logarithmically below the seismogenic zone. This may be driven by the fault friction related to lithological contrasts.

5. Special attention should be paid to the KF (particularly the Maqin segment and east of the Tuosuo Lake segment) and the central-western segment of the Bayan Har Shan Main Peak Fault for enhanced seismic hazard where we observed interseismic strain localization and positive stress loading (larger than 0.01 MPa) induced by the 2021 Maduo earthquake. The unruptured segment between the 2001 Kokoxili and 2021 Maduo events is also worth concern for elevated earthquake potential with comparable increased ΔCFS.

Data Availability Statement

The interferograms used in this study are downloadable from https://comet.nerc.ac.uk/comet-lics-portal/. The geodetic slip inversion code is publicly available at https://github.com/ruthamey/slipBERI. Coseismic slip models derived from InSAR and teleseismic data, interseismic eastward and vertical velocity and maximum shear strain rate fields are available at https://doi.org/10.5281/zenodo.7215161. The moment tensor solution of the 2021 Maduo earthquake comes from the Global Centroid Moment Tensor project (GCMT; https://www.globalcmt.org/CMTsearch.html). The facilities of IRIS Data Services, and specifically the IRIS Data Management Center, were used for access to waveforms, related metadata, and/or derived products used in this study. IRIS Data Services are funded through the Seismological Facilities for the Advancement of Geoscience (SAGE) Award of the National Science Foundation under Cooperative Support Agreement EAR-1851048. The seismic data were downloaded through the IRIS Wilber 3 system (https://ds.iris.edu/wilber3/find_event) or IRIS Web Services (https://service.iris.edu/), including the following seismic networks: the CN (Canadian National Seismograph Network (CNSN); Natural Resources Canada (NRCAN Canada), 1975), the CZ (Czech Regional Seismic Network (CZ); Charles University in Prague (Czech) et al., 1973), the G (GEOSCOPE; Institut De Physique Du Globe De Paris (IPGP) & Ecole Et Observatoire Des Sciences De La Terre De Strasbourg (EOST), 1982), the GE (GEOFON Seismic Network; GEOFON Data Centre, 1993), the II (IRIS/IDA Seismic Network; Scripps Institution Of Oceanography, 1986), the IM (International Miscellaneous Stations (IMS); International Miscellaneous Stations (IMS), 1965), the IU (Global Seismograph Network (GSN - IRIS/USGS); Albuquerque Seismological Laboratory (ASL)/USGS, 1988), the MN (Mediterranean Very Broadband Seismographic Network (MedNet); MedNet Project Partner Institutions, 1988), the NL (Netherlands Seismic and Acoustic Network (KNMI/ORFEUS); KNMI, 1993), and the PS (Pacific21 (ERI/STA); University of Tokyo Earthquake Research Institute (Todai ERI Japan), 1989).

Acknowledgments

This study was funded by the Natural Environment Research Council (NERC) through the "Looking inside the Continents from Space (LiCS)" large grants to Leeds (NE/K010867/1) and Oxford (NE/K011006/1) Universities. COMET is the UK NERC Centre for the Observation and Modelling of Earthquakes, Volcanoes and Tectonics, a partnership between UK Universities and the British Geological Survey. We acknowledge the support through a China Scholarship Council-University of Leeds joint scholarship awarded to Jin Fang (202006270022) and two University Research Fellowships from the Royal Society (UK) to Tim Craig (URF180088) and John Elliott (UF150282). We would like to thank Isabelle Manighetti, the editor, the associate editor, and three anonymous reviewers for their constructive comments. Ryo Okuwaki acknowledges Yuji Yagi and Kousuke Shimizu for helping with teleseismic inversion and their development of the method. Slip inversion was undertaken on ARC4, part of the High Performance Computing facilities at the University of Leeds, UK. LiCSAR contains modified Copernicus Sentinel data (2014-2021) analyzed by COMET. LiCSAR uses JASMIN, the UK's collaborative data analysis environment (http://jasmin.ac.uk). Figures were produced using the Generic Mapping Tools (GMT) (Wessel et al., 2013), Matlab and Python.

References

Akaike, H. (1980). Likelihood and the Bayes procedure. *Trabajos de Estadistica y de Investigacion Operativa*, *31*(1), 143–166. https://doi.org/10.1007/BF02888350

Albuquerque Seismological Laboratory (ASL)/USGS. (1988). *Global seismograph network (GSN—IRIS/USGS)*. International Federation of Digital Seismograph Networks. https://doi.org/10.7914/SN/IU

Amey, R. M. J., Hooper, A., & Walters, R. J. (2018). A Bayesian method for incorporating self-similarity into earthquake slip inversions. *Journal of Geophysical Research: Solid Earth*, *123*(7), 6052–6071. https://doi.org/10.1029/2017JB015316

Ampuero, J.-P., & Dahlen, F. A. (2005). Ambiguity of the moment tensor. *Bulletin of the Seismological Society of America*, *95*(2), 390–400. https://doi.org/10.1785/0120040103

Anderson, J. G., Wesnousky, S. G., & Stirling, M. W. (1996). Earthquake size as a function of fault slip rate. *Bulletin of the Seismological Society of America*, *86*(3), 683–690. https://doi.org/10.1785/BSSA0860030683

Aviles, C. A., Scholz, C. H., & Boatwright, J. (1987). Fractal analysis applied to characteristic segments of the San Andreas Fault. *Journal of Geophysical Research*, *92*(B1), 331–344. https://doi.org/10.1029/JB092iB01p00331

Avouac, J.-P. (2015). From geodetic imaging of seismic and aseismic fault slip to dynamic modeling of the seismic cycle. *Annual Review of Earth and Planetary Sciences*, *43*(1), 233–271. https://doi.org/10.1146/annurev-earth-060614-105302

Avouac, J.-P., & Tapponnier, P. (1993). Kinematic model of active deformation in central Asia. *Geophysical Research Letters*, *20*(10), 895–898. https://doi.org/10.1029/93GL00128

Bao, H., Ampuero, J.-P., Meng, L., Fielding, E. J., Liang, C., Milliner, C. W. D., et al. (2019). Early and persistent supershear rupture of the 2018 magnitude 7.5 Palu earthquake. *Nature Geoscience*, *12*(3), 200–205. https://doi.org/10.1038/s41561-018-0297-z

Bedford, J., Moreno, M., Baez, J. C., Lange, D., Tilmann, F., Rosenau, M., et al. (2013). A high-resolution, time-variable afterslip model for the 2010 Maule Mw = 8.8, Chile megathrust earthquake. *Earth and Planetary Science Letters*, *383*, 26–36. https://doi.org/10.1016/j.epsl.2013.09.020

Ben-Zion, Y. (2008). Collective behavior of earthquakes and faults: Continuum-discrete transitions, progressive evolutionary changes, and different dynamic regimes. *Reviews of Geophysics*, *46*(4), RG4006. https://doi.org/10.1029/2008RG000260

Ben-Zion, Y., & Sammis, C. G. (2003). Characterization of fault zones. *Pure and Applied Geophysics*, *160*(3), 677–715. https://doi.org/10.1007/PL00012554

Boatwright, J., & Cocco, M. (1996). Frictional constraints on crustal faulting. *Journal of Geophysical Research*, *101*(B6), 13895–13909. https://doi.org/10.1029/96JB00405

Byerlee, J. D., & Brace, W. F. (1968). Stick slip, stable sliding, and earthquakes—Effect of rock type, pressure, strain rate, and stiffness. *Journal of Geophysical Research*, *73*(18), 6031–6037. https://doi.org/10.1029/JB073i018p06031

Calais, E., & Stein, S. (2009). Time-variable deformation in the new Madrid seismic zone. *Science*, *323*(5920), 1442. https://doi.org/10.1126/science.1168122

Carpenter, B. M., Saffer, D. M., & Marone, C. (2012). Frictional properties and sliding stability of the San Andreas fault from deep drill core. *Geology*, *40*(8), 759–762. https://doi.org/10.1130/G33007.1

Carpenter, B. M., Saffer, D. M., & Marone, C. (2015). Frictional properties of the active San Andreas Fault at SAFOD: Implications for fault strength and slip behavior. *Journal of Geophysical Research: Solid Earth*, *120*(7), 5273–5289. https://doi.org/10.1002/2015JB011963

Cesca, S., Zhang, Y., Mouslopoulou, V., Wang, R., Saul, J., Savage, M., et al. (2017). Complex rupture process of the Mw 7.8, 2016, Kaikoura earthquake, New Zealand, and its aftershock sequence. *Earth and Planetary Science Letters*, *478*, 110–120. https://doi.org/10.1016/j.epsl.2017.08.024

Cetin, E., Cakir, Z., Meghraoui, M., Ergintav, S., & Akoglu, A. M. (2014). Extent and distribution of aseismic slip on the Ismetpaşa segment of the north Anatolian Fault (Turkey) from Persistent Scatterer InSAR. *Geochemistry, Geophysics, Geosystems*, *15*(7), 2883–2894. https://doi.org/10.1002/2014GC005307

Charles University in Prague (Czech). (1973). *Czech regional seismic network. International federation of digital seismograph networks*. Institute of Geonics, Institute of Geophysics, Academy of Sciences of the Czech Republic, Institute of Physics of the Earth Masaryk University (Czech), & Institute of Rock Structure and Mechanics. https://doi.org/10.7914/SN/CZ

Chen, C. W., & Zebker, H. A. (2000). Network approaches to two-dimensional phase unwrapping: Intractability and two new algorithms. *Journal of the Optical Society of America A*, *17*(3), 401–414. https://doi.org/10.1364/JOSAA.17.000401

Chen, C. W., & Zebker, H. A. (2001). Two-dimensional phase unwrapping with use of statistical models for cost functions in nonlinear optimization. *Journal of the Optical Society of America A*, *18*(2), 338–351. https://doi.org/10.1364/JOSAA.18.000338

Chen, C. W., & Zebker, H. A. (2002). Phase unwrapping for large SAR interferograms: Statistical segmentation and generalized network models. *IEEE Transactions on Geoscience and Remote Sensing*, *40*(8), 1709–1719. https://doi.org/10.1109/TGRS.2002.802453

Chen, H., Qu, C., Zhao, D., Ma, C., & Shan, X. (2021). Rupture kinematics and coseismic slip model of the 2021 Mw 7.3 Maduo (China) Earthquake: Implications for the seismic hazard of the Kunlun fault. *Remote Sensing*, *13*(16), 3327. https://doi.org/10.3390/rs13163327

Chen, K., Avouac, J.-P., Geng, J., Liang, C., Zhang, Z., Li, Z., & Zhang, S. (2022). The 2021 Mw 7.4 Madoi earthquake: An archetype bilateral slip-pulse rupture arrested at a splay fault. *Geophysical Research Letters*, *49*(2), e2021GL095243. https://doi.org/10.1029/2021GL095243

Chen, Q., Freymueller, J. T., Wang, Q., Yang, Z., Xu, C., & Liu, J. (2004). A deforming block model for the present-day tectonics of Tibet. *Journal of Geophysical Research*, *109*(B1), B01403. https://doi.org/10.1029/2002JB002151

Chen, S. F., Wilson, C., Deng, Q. D., Zhao, X. L., & Zhi, L. L. (1994). Active faulting and block movement associated with large earthquakes in the Min Shan and Longmen Mountains, northeastern Tibetan Plateau. *Journal of Geophysical Research*, *99*(B12), 24025–24038. https://doi.org/10.1029/94JB02132

Chen, Z., Burchfiel, B. C., Liu, Y., King, R. W., Royden, L. H., Tang, W., et al. (2000). Global positioning system measurements from eastern Tibet and their implications for India/Eurasia intercontinental deformation. *Journal of Geophysical Research*, *105*(B7), 16215–16227. https://doi.org/10.1029/2000JB900092

Cheng, J., Liu, J., Xu, X.-w., & Gan, W.-j. (2014). Tectonic characteristics of strong earthquakes in daliangshan sub-block and impact of the Ms6.5 Ludian earthquake in 2014 on the surrounding faults. *Seismology and Geology*, *36*(4), 1228–1243. https://doi.org/10.3969/j.issn.0253-4967.2014.04.023

Chlieh, M., Avouac, J.-P., Hjorleifsdottir, V., Song, T.-R. A., Ji, C., Sieh, K., et al. (2007). Coseismic slip and afterslip of the great Mw 9.15 Sumatra–Andaman earthquake of 2004. *Bulletin of the Seismological Society of America*, *97*(1A), S152–S173. https://doi.org/10.1785/0120050631

Coleman, M., & Hodges, K. (1995). Evidence for Tibetan plateau uplift before 14 Myr ago from a new minimum age for east–west extension. *Nature*, *374*(6517), 49–52. https://doi.org/10.1038/374049a0

Collettini, C., Niemeijer, A., Viti, C., & Marone, C. (2009). Fault zone fabric and fault weakness. *Nature*, *462*(7275), 907–910. https://doi.org/10.1038/nature08585

Crider, J. G., & Peacock, D. C. P. (2004). Initiation of brittle faults in the upper crust: A review of field observations. *Journal of Structural Geology*, *26*(4), 691–707. https://doi.org/10.1016/j.jsg.2003.07.007

Daout, S., Doin, M.-P., Peltzer, G., Lasserre, C., Socquet, A., Volat, M., & Sudhaus, H. (2018). Strain partitioning and present-day fault kinematics in NW Tibet from envisat SAR interferometry. *Journal of Geophysical Research: Solid Earth*, *123*(3), 2462–2483. https://doi.org/10.1002/2017JB015020

Deng, Q., Zhang, P.-z., Ran, Y.-k., Yang, X., Min, W., & Chen, L.-c. (2003). Active tectonics and earthquake activities in China. *Earth Science Frontiers*, *10*(S1), 66–73.

Deng, Q.-D., Cheng, S.-P., Ji, M. A., & Peng, D. U. (2014). Seismic activities and earthquake potential in the Tibetan Plateau. *Chinese Journal of Geophysics*, *57*(5), 678–697. https://doi.org/10.1002/cjg2.20133

Diao, F., Xiong, X., Wang, R., Walter, T. R., Wang, Y., & Wang, K. (2019). Slip rate variation along the Kunlun fault (Tibet): Results from new GPS observations and a viscoelastic earthquake-cycle deformation model. *Geophysical Research Letters*, *46*(5), 2524–2533. https://doi.org/10.1029/2019GL081940

Dokka, R. K., & Travis, C. J. (1990a). Late Cenozoic strike-slip faulting in the Mojave Desert, California. *Tectonics*, *9*(2), 311–340. https://doi.org/10.1029/TC009i002p00311

Dokka, R. K., & Travis, C. J. (1990b). Role of the eastern California shear zone in accommodating Pacific-North American Plate motion. *Geophysical Research Letters*, *17*(9), 1323–1326. https://doi.org/10.1029/GL017i009p01323

Dolan, J. F., Bowman, D. D., & Sammis, C. G. (2007). Long-range and long-term fault interactions in Southern California. *Geology*, *35*(9), 855–858. https://doi.org/10.1130/G23789A.1

Dong, P., Zhao, B., & Qiao, X. (2022). Interaction between historical earthquakes and the 2021 Mw7.4 Maduo event and their impacts on the seismic gap areas along the East Kunlun fault. *Earth Planets and Space*, *74*(1), 42. https://doi.org/10.1186/s40623-022-01589-3

Dziewonski, A. M., Chou, T. A., & Woodhouse, J. H. (1981). Determination of earthquake source parameters from waveform data for studies of global and regional seismicity. *Journal of Geophysical Research*, *86*(B4), 2825–2852. https://doi.org/10.1029/JB086iB04p02825

Ekström, G., Nettles, M., & Dziewoński, A. (2012). The global CMT project 2004–2010: Centroid-moment tensors for 13, 017 earthquakes. *Physics of the Earth and Planetary Interiors*, *200*, 1–9. https://doi.org/10.1016/j.pepi.2012.04.002

Elliott, J., Walters, R., & Wright, T. (2016). The role of space-based observation in understanding and responding to active tectonics and earthquakes. *Nature Communications*, *7*(1), 1–16. https://doi.org/10.1038/ncomms13844

England, P., & McKenzie, D. (1982). A thin viscous sheet model for continental deformation. *Geophysical Journal International*, *70*(2), 295–321. https://doi.org/10.1111/j.1365-246x.1982.tb04969.x

Fagereng, Å., & Sibson, R. H. (2010). Mélange rheology and seismic style. *Geology*, *38*(8), 751–754. https://doi.org/10.1130/G30868.1

Floyd, M. A., Walters, R. J., Elliott, J. R., Funning, G. J., Svarc, J. L., Murray, J. R., et al. (2016). Spatial variations in fault friction related to lithology from rupture and afterslip of the 2014 South Napa, California, earthquake. *Geophysical Research Letters*, *43*(13), 6808–6816. https://doi.org/10.1002/2016GL069428

Fukahata, Y., & Wright, T. J. (2008). A non-linear geodetic data inversion using ABIC for slip distribution on a fault with an unknown dip angle. *Geophysical Journal International*, *173*(2), 353–364. https://doi.org/10.1111/j.1365-246X.2007.03713.x

Fukuda, J., & Johnson, K. M. (2008). A fully Bayesian inversion for spatial distribution of fault slip with objective smoothing. *Bulletin of the Seismological Society of America*, *98*(3), 1128–1146. https://doi.org/10.1785/0120070194

Funning, G. J., Parsons, B., & Wright, T. J. (2007). Fault slip in the 1997 Manyi, Tibet earthquake from linear elastic modelling of InSAR displacements. *Geophysical Journal International*, *169*(3), 988–1008. https://doi.org/10.1111/j.1365-246x.2006.03318.x

Galli, P. A. C., & Peronace, E. (2015). Low slip rates and multimillennial return times for Mw 7 earthquake faults in southern Calabria (Italy). *Geophysical Research Letters*, *42*(13), 5258–5265. https://doi.org/10.1002/2015GL064062

GEOFON Data Centre. (1993). GEOFON seismic network. *Deutsches GeoForschungsZentrum GFZ*. https://doi.org/10.14470/TR560404

Goldberg, D. E., Melgar, D., Sahakian, V. J., Thomas, A. M., Xu, X., Crowell, B. W., & Geng, J. (2020). Complex rupture of an immature fault zone: A simultaneous kinematic model of the 2019 ridgecrest, CA earthquakes. *Geophysical Research Letters*, *47*(3), e2019GL086382. https://doi.org/10.1029/2019GL086382

Gomberg, J., Reasenberg, P. A., Bodin, P., & Harris, R. A. (2001). Earthquake triggering by seismic waves following the landers and hector mine earthquakes. *Nature*, *411*(6836), 462–466. https://doi.org/10.1038/35078053

Gombert, B., Duputel, Z., Jolivet, R., Doubre, C., Rivera, L., & Simons, M. (2018). Revisiting the 1992 landers earthquake: A Bayesian exploration of co-seismic slip and off-fault damage. *Geophysical Journal International*, *212*(2), 839–852. https://doi.org/10.1093/gji/ggx455

Gratier, J. P., Richard, J., Renard, F., Mittempergher, S., Doan, M. L., Di Toro, G., et al. (2011). Aseismic sliding of active faults by pressure solution creep: Evidence from the San Andreas Fault observatory at depth. *Geology*, *39*(12), 1131–1134. https://doi.org/10.1130/G32073.1

Guo, R., Yang, H., Li, Y., Zheng, Y., & Zhang, L. (2021). Complex slip distribution of the 2021 Mw 7.4 Maduo, China, Earthquake: An event occurring on the slowly slipping fault. *Seismological Research Letters*, *93*(2A), 653–665. https://doi.org/10.1785/0220210226

Ha, G., Liu, J., Ren, Z., Zhu, X., Bao, G., Wu, D., & Zhang, Z. (2022). The interpretation of seismogenic fault of the Maduo Mw 7.3 Earthquake, Qinghai based on remote sensing images—A branch of the East Kunlun fault system. *Journal of Earth Science*, *33*(4), 857–868. https://doi.org/10.1007/s12583-021-1556-2

Hamling, I. J., Hreinsdóttir, S., Clark, K., Elliott, J., Liang, C., Fielding, E., et al. (2017). Complex multifault rupture during the 2016 Mw 7.8 Kaikōura earthquake, New Zealand. *Science*, *356*(6334), eaam7194. https://doi.org/10.1126/science.aam7194

Harris, R. A. (2017). Large earthquakes and creeping faults. *Reviews of Geophysics*, *55*(1), 169–198. https://doi.org/10.1002/2016RG000539

Hauksson, E., Jones, L. M., Hutton, K., & Eberhart-Phillips, D. (1993). The 1992 Landers earthquake sequence: Seismological observations. *Journal of Geophysical Research*, *98*(B11), 19835–19858. https://doi.org/10.1029/93JB02384

He, K., Wen, Y., Xu, C., & Zhao, Y. (2021). Fault geometry and slip distribution of the 2021 Mw 7.4 Maduo, China, earthquake inferred from InSAR measurements and relocated aftershocks. *Seismological Research Letters*, *93*(1), 8–20. https://doi.org/10.1785/0220210204

He, L., Feng, G., Wu, X., Lu, H., Xu, W., Wang, Y., et al. (2021). Coseismic and early postseismic slip models of the 2021 Mw 7.4 Maduo earthquake (Western China) estimated by space-based geodetic data. *Geophysical Research Letters*, *48*(24), e2021GL095860. https://doi.org/10.1029/2021GL095860

Hicks, S. P., Okuwaki, R., Steinberg, A., Rychert, C. A., Harmon, N., Abercrombie, R. E., et al. (2020). Back-propagating supershear rupture in the 2016 Mw 7.1 Romanche transform fault earthquake. *Nature Geoscience*, *13*(9), 647–653. https://doi.org/10.1038/s41561-020-0619-9

Hong, S., Liu, M., Liu, T., Dong, Y., Chen, L., Meng, G., & Xu, Y. (2022). Fault source model and stress changes of the 2021 Mw 7.4 Maduo Earthquake, China, constrained by InSAR and GPS measurements. *Bulletin of the Seismological Society of America*, *112*(3), 1284–1296. https://doi.org/10.1785/0120210250

Hu, Y., Yagi, Y., Okuwaki, R., & Shimizu, K. (2021). Back-propagating rupture evolution within a curved slab during the 2019 Mw 8.0 Peru intraslab earthquake. *Geophysical Journal International*, *227*(3), 1602–1611. https://doi.org/10.1093/gji/ggab303

Hussain, E., Wright, T. J., Walters, R. J., Bekaert, D., Hooper, A., & Houseman, G. A. (2016). Geodetic observations of postseismic creep in the decade after the 1999 Izmit earthquake, Turkey: Implications for a shallow slip deficit. *Journal of Geophysical Research: Solid Earth*, *121*(4), 2980–3001. https://doi.org/10.1002/2015JB012737

Hussain, E., Wright, T. J., Walters, R. J., Bekaert, D. P., Lloyd, R., & Hooper, A. (2018). Constant strain accumulation rate between major earthquakes on the North Anatolian Fault. *Nature Communications*, *9*(1), 1–9. https://doi.org/10.1038/s41467-018-03739-2

Institut De Physique Du Globe De Paris (IPGP)Ecole Et Observatoire Des Sciences De La Terre De Strasbourg (EOST). (1982). *GEOSCOPE, French global network of broad band seismic stations*. Institut de physique du globe de Paris (IPGP). https://doi.org/10.18715/GEOSCOPE.G

International Miscellaneous Stations (IMS). (1965). International miscellaneous stations (IMS). Retrieved from https://www.fdsn.org/networks/detail/IM/

Irwin, W. P., & Barnes, I. (1975). Effect of geologic structure and metamorphic fluids on seismic behavior of the San Andreas Fault system in central and northern California. *Geology*, *3*(12), 713–716. https://doi.org/10.1130/0091-7613(1975)3<713:eogsam>2.0.co;2

Ji, C., Wald, D. J., & Helmberger, D. V. (2002). Source description of the 1999 Hector Mine, California, Earthquake, Part I: Wavelet domain inversion theory and resolution analysis. *Bulletin of the Seismological Society of America*, *92*(4), 1192–1207. https://doi.org/10.1785/0120000916

Jin, Z., & Fialko, Y. (2021a). Coseismic and early postseismic deformation due to the 2021 M7. 4 Maduo (Tibet, China) earthquake. *AGU Fall Meeting Abstracts*, *2021*, S55F–S0205.

Jin, Z., & Fialko, Y. (2021b). Coseismic and early postseismic deformation due to the 2021 M7.4 Maduo (China) earthquake. *Geophysical Research Letters*, *48*(21), e2021GL095213. https://doi.org/10.1029/2021GL095213

Jolivet, R., Lasserre, C., Doin, M. P., Peltzer, G., Avouac, J. P., Sun, J., & Dailu, R. (2013). Spatio-temporal evolution of aseismic slip along the Haiyuan fault, China: Implications for fault frictional properties. *Earth and Planetary Science Letters*, *377–378*, 23–33. https://doi.org/10.1016/j.epsl.2013.07.020

Jolivet, R., Simons, M., Agram, P. S., Duputel, Z., & Shen, Z.-K. (2015). Aseismic slip and seismogenic coupling along the central San Andreas Fault. *Geophysical Research Letters*, *42*(2), 297–306. https://doi.org/10.1002/2014GL062222

Kennett, B. L. N., Engdahl, E. R., & Buland, R. (1995). Constraints on seismic velocities in the Earth from traveltimes. *Geophysical Journal International*, *122*(1), 108–124. https://doi.org/10.1111/j.1365-246X.1995.tb03540.x

Khazaradze, G., & Klotz, J. (2003). Short- and long-term effects of GPS measured crustal deformation rates along the south central Andes. *Journal of Geophysical Research*, *108*(B6), 2289. https://doi.org/10.1029/2002JB001879

Kikuchi, M., & Kanamori, H. (1991). Inversion of complex body waves—III. *Bulletin of the Seismological Society of America*, *81*(6), 2335–2350. https://doi.org/10.1785/BSSA0810062335

KNMI. (1993). *Netherlands seismic and acoustic network*. Royal Netherlands Meteorological Institute (KNMI). https://doi.org/10.21944/E970FD34-23B9-3411-B366-E4F72877D2C5

Laske, G., Masters, G., Ma, Z., & Pasyanos, M. (2013). Update on CRUST1. 0—A 1-degree global model of Earth's crust [Conference Proceedings]. *Geophysical Research Abstracts*, *15*, 2658. Retrieved from https://meetingorganizer.copernicus.org/EGU2013/EGU2013-2658.pdf

Lasserre, C., Peltzer, G., Crampé, F., Klinger, Y., Van der Woerd, J., & Tapponnier, P. (2005). Coseismic deformation of the 2001 Mw = 7.8 Kokoxili earthquake in Tibet, measured by synthetic aperture radar interferometry. *Journal of Geophysical Research*, *110*(B12), B12408. https://doi.org/10.1029/2004JB003500

Lazecký, M., Spaans, K., González, P. J., Maghsoudi, Y., Morishita, Y., Albino, F., et al. (2020). LiCSAR: An automatic InSAR tool for measuring and monitoring tectonic and volcanic activity. *Remote Sensing*, *12*(15), 2430. https://doi.org/10.3390/rs12152430

Li, C., Li, T., Shan, X., & Zhang, G. (2022). Extremely large off-fault deformation during the 2021 Mw 7.4 Maduo, Tibetan Plateau, earthquake. *Seismological Research Letters*. https://doi.org/10.1785/0220220139

Li, H., Shen, Y., Huang, Z., Li, X., Gong, M., Shi, D., et al. (2014). The distribution of the mid-to-lower crustal low-velocity zone beneath the northeastern Tibetan Plateau revealed from ambient noise tomography. *Journal of Geophysical Research: Solid Earth*, *119*(3), 1954–1970. https://doi.org/10.1002/2013JB010374

Li, K., Xu, X., Wei, L., Wang, Q., & Shu, P. (2019). Evidence of long recurrence times and low slip rate along the 1668 Tancheng earthquake fault. *Chinese Science Bulletin*, *64*(11), 1168–1178. https://doi.org/10.1360/N972018-00961

Li, Q., Wan, Y., Li, C., Tang, H., Tan, K., & Wang, D. (2022). Source process featuring asymmetric rupture velocities of the 2021 Mw 7.4 Maduo, China, earthquake from teleseismic and geodetic data. *Seismological Research Letters*, *93*(3), 1429–1439. https://doi.org/10.1785/0220210300

Li, Y., Jia, D., Wang, M., Shaw, J. H., He, J., Lin, A., et al. (2014). Structural geometry of the source region for the 2013 Mw 6.6 Lushan earthquake: Implication for earthquake hazard assessment along the Longmen Shan. *Earth and Planetary Science Letters*, *390*, 275–286. https://doi.org/10.1016/j.epsl.2014.01.018

Li, Z., Elliott, J. R., Feng, W., Jackson, J. A., Parsons, B. E., & Walters, R. J. (2011). The 2010 MW 6.8 Yushu (Qinghai, China) earthquake: Constraints provided by InSAR and body wave seismology. *Journal of Geophysical Research*, *116*(B10), B10302. https://doi.org/10.1029/2011JB008358

Li, Z., Fielding, E. J., & Cross, P. (2009). Integration of InSAR time-series analysis and water-vapor correction for mapping postseismic motion after the 2003 Bam (Iran) Earthquake. *IEEE Transactions on Geoscience and Remote Sensing*, *47*(9), 3220–3230. https://doi.org/10.1109/TGRS.2009.2019125

Li, Z., Li, W., Li, T., Xu, Y., Su, P., Guo, P., et al. (2021). Seismogenic fault and coseismic surface deformation of the Maduo Ms7. 4 earthquake in Qinghai, China: A quick report. *Seismology and Geology*, *43*(3), 722–737. https://doi.org/10.3969/j.issn.0253-4967.2021.03.016

Liang, S., Gan, W., Shen, C., Xiao, G., Liu, J., Chen, W., et al. (2013). Three-dimensional velocity field of present-day crustal motion of the Tibetan Plateau derived from GPS measurements. *Journal of Geophysical Research: Solid Earth*, *118*(10), 5722–5732. https://doi.org/10.1002/2013JB010503

Liu, F., Elliott, J. R., Craig, T. J., Hooper, A., & Wright, T. J. (2021). Improving the resolving power of InSAR for earthquakes using time series: A case study in Iran. *Geophysical Research Letters*, *48*(14), e2021GL093043. https://doi.org/10.1029/2021GL093043

Liu, J., Hu, J., Li, Z., Ma, Z., Wu, L., Jiang, W., et al. (2022). Complete three-dimensional coseismic displacements due to the 2021 Maduo earthquake in Qinghai Province, China from Sentinel-1 and ALOS-2 SAR images. *Science China Earth Sciences*, *65*(4), 687–697. https://doi.org/10.1007/s11430-021-9868-9

Liu, L., Li, Y., Zhu, L., & Ji, L. (2021). Influence of the 1947 Dari M7.7 earthquake on stress evolution along the boundary fault of the Bayan Har block: Insights from numerical simulation. *Chinese Journal of Geophysics*, *64*(7), 2221–2231. https://doi.org/10.6038/cjg2021P0194

Liu-Zeng, J., Zhang, Z., Rollins, C., Gualandi, A., Avouac, J. P., Shi, H., et al. (2020). Postseismic deformation following the 2015 Mw7.8 Gorkha (Nepal) earthquake: New GPS data, kinematic and dynamic models, and the roles of afterslip and viscoelastic relaxation. *Journal of Geophysical Research: Solid Earth*, *125*(9), e2020JB019852. https://doi.org/10.1029/2020JB019852

Lohman, R. B., & Simons, M. (2005). Some thoughts on the use of InSAR data to constrain models of surface deformation: Noise structure and data downsampling. *Geochemistry, Geophysics, Geosystems*, *6*(1), Q01007. https://doi.org/10.1029/2004GC000841

Loveless, J. P., & Meade, B. J. (2011). Partitioning of localized and diffuse deformation in the Tibetan Plateau from joint inversions of geologic and geodetic observations. *Earth and Planetary Science Letters*, *303*(1), 11–24. https://doi.org/10.1016/j.epsl.2010.12.014

MacQueen, P., Delgado, F., Reath, K., Pritchard, M. E., Bagnardi, M., Milillo, P., et al. (2020). Volcano-tectonic interactions at sabancaya volcano, Peru: Eruptions, magmatic inflation, moderate earthquakes, and fault creep. *Journal of Geophysical Research: Solid Earth*, *125*(5), e2019JB019281. https://doi.org/10.1029/2019JB019281

Mai, P. M., & Beroza, G. C. (2002). A spatial random field model to characterize complexity in earthquake slip. *Journal of Geophysical Research*, *107*(B11), ESE10-1–ESE10-21. https://doi.org/10.1029/2001JB000588

Manighetti, I., Campillo, M., Bouley, S., & Cotton, F. (2007). Earthquake scaling, fault segmentation, and structural maturity. *Earth and Planetary Science Letters*, *253*(3), 429–438. https://doi.org/10.1016/j.epsl.2006.11.004

Manighetti, I., Mercier, A., & De Barros, L. (2021). Fault trace corrugation and segmentation as a measure of fault structural maturity. *Geophysical Research Letters*, *48*(20), e2021GL095372. https://doi.org/10.1029/2021GL095372

Marone, C. (1998). Laboratory-derived friction laws and their application to seismic faulting. *Annual Review of Earth and Planetary Sciences*, *26*(1), 643–696. https://doi.org/10.1146/annurev.earth.26.1.643

Marone, C. J., Scholtz, C. H., & Bilham, R. (1991). On the mechanics of earthquake afterslip. *Journal of Geophysical Research*, *96*(B5), 8441–8452. https://doi.org/10.1029/91JB00275

Massonnet, D., Rossi, M., Carmona, C., Adragna, F., Peltzer, G., Feigl, K., & Rabaute, T. (1993). The displacement field of the Landers earthquake mapped by radar interferometry. *Nature*, *364*(6433), 138–142. https://doi.org/10.1038/364138a0

Mavko, G. M. (1982). Fault interaction near Hollister, California. *Journal of Geophysical Research*, *87*(B9), 7807–7816. https://doi.org/10.1029/JB087iB09p07807

McCaffrey, R., Long, M. D., Goldfinger, C., Zwick, P. C., Nabelek, J. L., Johnson, C. K., & Smith, C. (2000). Rotation and plate locking at the Southern Cascadia Subduction zone. *Geophysical Research Letters*, *27*(19), 3117–3120. https://doi.org/10.1029/2000GL011768

McClusky, S. C., Bjornstad, S. C., Hager, B. H., King, R. W., Meade, B. J., Miller, M. M., et al. (2001). Present day kinematics of the Eastern California Shear Zone from a geodetically constrained block model. *Geophysical Research Letters*, *28*(17), 3369–3372. https://doi.org/10.1029/2001GL013091

Meade, B. J., & Hager, B. H. (2005). Block models of crustal motion in southern California constrained by GPS measurements. *Journal of Geophysical Research*, *110*(B3), B03403. https://doi.org/10.1029/2004JB003209

MedNet Project Partner Institutions. (1988). Mediterranean very broadband seismographic network (mednet). Istituto Nazionale di Geofisica e Vulcanologia (INGV). https://doi.org/10.13127/SD/FBBBTDTD6Q

Molnar, P., & Tapponnier, P. (1978). Active tectonics of Tibet. *Journal of Geophysical Research*, *83*(B11), 5361–5375. https://doi.org/10.1029/JB083iB11p05361

Morishita, Y. (2021). Nationwide urban ground deformation monitoring in Japan using Sentinel-1 LiCSAR products and LiCSBAS. *Progress in Earth and Planetary Science*, *8*(1), 6. https://doi.org/10.1186/s40645-020-00402-7

Morishita, Y., Lazecky, M., Wright, T. J., Weiss, J. R., Elliott, J. R., & Hooper, A. (2020). LiCSBAS: An open-source InSAR time series analysis package integrated with the LiCSAR automated Sentinel-1 InSAR processor. *Remote Sensing*, *12*(3), 424. https://doi.org/10.3390/rs12030424

Murphy, B., Müller, S., & Yurchak, R. (2021). GeoStat-framework/PyKrige: V1.6.1 (v1.6.1). *Zenodo*. https://doi.org/10.5281/zenodo.5380342

Natural Resources Canada (NRCAN Canada). (1975). Canadian national seismograph network. international federation of digital seismograph networks. https://doi.org/10.7914/SN/CN

Newman, A., Stein, S., Weber, J., Engeln, J., Mao, A., & Dixon, T. (1999). Slow deformation and lower seismic hazard at the new Madrid seismic zone. *Science*, *284*(5414), 619–621. https://doi.org/10.1126/science.284.5414.619

Nishimura, T. (2014). Pre-co-and post-seismic deformation of the 2011 Tohoku-oki earthquake and its implication to a paradox in short-term and long-term deformation. *Journal of Disaster Research*, *9*(3), 294–302. https://doi.org/10.20965/jdr.2014.p0294

Okada, Y. (1985). Surface deformation due to shear and tensile faults in a half-space. *Bulletin of the Seismological Society of America*, *75*(4), 1135–1154. https://doi.org/10.1785/BSSA0750041135

Okuwaki, R., Hicks, S. P., Craig, T. J., Fan, W., Goes, S., Wright, T. J., & Yagi, Y. (2021). Illuminating a contorted slab with a complex Intraslab rupture evolution during the 2021 Mw 7.3 East Cape, New Zealand earthquake. *Geophysical Research Letters*, *48*(24), e2021GL095117. https://doi.org/10.1029/2021GL095117

Okuwaki, R., Hirano, S., Yagi, Y., & Shimizu, K. (2020). Inchworm-like source evolution through a geometrically complex fault fueled persistent supershear rupture during the 2018 Palu Indonesia earthquake. *Earth and Planetary Science Letters*, *547*, 116449. https://doi.org/10.1016/j.epsl.2020.116449

Okuwaki, R., Yagi, Y., Aránguiz, R., González, J., & González, G. (2016). Rupture process during the 2015 Illapel, Chile earthquake: Zigzag-along-dip rupture episodes. *Pure and Applied Geophysics*, *173*(4), 1011–1020. https://doi.org/10.1007/s00024-016-1271-6

Ou, Q., Daout, S., Weiss, J. R., Shen, L., Lazecký, M., Wright, T. J., & Parsons, B. E. (2022). Large-scale interseismic strain mapping of the NE Tibetan Plateau from Sentinel-1 interferometry. *Journal of Geophysical Research: Solid Earth*, *127*(6), e2022JB024176. https://doi.org/10.1029/2022JB024176

Ozacar, A. A., & Beck, S. L. (2004). The 2002 Denali fault and 2001 Kunlun fault earthquakes: Complex rupture processes of two large strike-slip events. *Bulletin of the Seismological Society of America*, *94*(6B), S278–S292. https://doi.org/10.1785/0120040604

Pagani, C., Bodin, T., Métois, M., & Lasserre, C. (2021). Bayesian estimation of surface strain rates from global navigation satellite system measurements: Application to the Southwestern United States. *Journal of Geophysical Research: Solid Earth*, *126*(6), 1–25. https://doi.org/10.1029/2021JB021905

Pajang, S., Cubas, N., Letouzey, J., Le Pourhiet, L., Seyedali, S., Fournier, M., et al. (2021). Seismic hazard of the western Makran subduction zone: Insight from mechanical modelling and inferred frictional properties. *Earth and Planetary Science Letters*, *562*, 116789. https://doi.org/10.1016/j.epsl.2021.116789

Pan, J., Bai, M., Li, C., Liu, F., Li, H., Liu, D., et al. (2021). Coseismic surface rupture and seismogenic structure of the 2021-05-22 Maduo (Qinghai) Ms 7.4 earthquake. *Acta Geologica Sinica*, *95*(6), 1655–1670. https://doi.org/10.19762/j.cnki.dizhixuebao.2021166

Pan, J., Li, H., Chevalier, M.-L., Tapponnier, P., Bai, M., Li, C., et al. (2022). Co-seismic rupture of the 2021, Mw7.4 Maduo earthquake (northern Tibet): Short-cutting of the Kunlun fault big bend. *Earth and Planetary Science Letters*, *594*, 117703. https://doi.org/10.1016/j.epsl.2022.117703

Pang, J., Ding, X., Han, K., Zeng, Y., Chen, A., Zhang, Y., et al. (2017a). The national 1: 1000000 geological map spatial database. *Geology in China*, *44*(S1), 8–18. https://doi.org/10.12029/gc2017Z102

Pang, J., Ding, X., Han, K., Zeng, Y., Chen, A., Zhang, Y., et al. (2017b). *The national 1: 1000000 geological map spatial database*. Geoscientific Data Discovery Publishing System. https://doi.org/10.23650/data.H.2017.NGA105570.T1.64.1

Passelègue, F. X., Schubnel, A., Nielsen, S., Bhat, H. S., Deldicque, D., & Madariaga, R. (2016). Dynamic rupture processes inferred from laboratory microearthquakes. *Journal of Geophysical Research: Solid Earth*, *121*(6), 4343–4365. https://doi.org/10.1002/2015JB012694

Peltzer, G., Crampé, F., & King, G. (1999). Evidence of nonlinear elasticity of the crust from the Mw7.6 Manyi (Tibet) earthquake. *Science*, *286*(5438), 272–276. https://doi.org/10.1126/science.286.5438.272

Peng, Z., & Gomberg, J. (2010). An integrated perspective of the continuum between earthquakes and slow-slip phenomena. *Nature Geoscience*, *3*(9), 599–607. https://doi.org/10.1038/ngeo940

Perrin, C., Manighetti, I., Ampuero, J.-P., Cappa, F., & Gaudemer, Y. (2016). Location of largest earthquake slip and fast rupture controlled by along-strike change in fault structural maturity due to fault growth. *Journal of Geophysical Research: Solid Earth*, *121*(5), 3666–3685. https://doi.org/10.1002/2015JB012671

Peyrat, S., Olsen, K., & Madariaga, R. (2001). Dynamic modeling of the 1992 Landers earthquake. *Journal of Geophysical Research*, *106*(B11), 26467–26482. https://doi.org/10.1029/2001JB000205

Powers, P. M., & Jordan, T. H. (2010). Distribution of seismicity across strike-slip faults in California. *Journal of Geophysical Research*, *115*(B5), B05305. https://doi.org/10.1029/2008JB006234

Radiguet, M., Cotton, F., Manighetti, I., Campillo, M., & Douglas, J. (2009). Dependency of near-field ground motions on the structural maturity of the ruptured faults. *Bulletin of the Seismological Society of America*, *99*(4), 2572–2581. https://doi.org/10.1785/0120080340

Reinen, L. A., Tullis, T. E., & Weeks, J. D. (1992). Two-mechanism model for frictional sliding of serpentinite. *Geophysical Research Letters*, *19*(15), 1535–1538. https://doi.org/10.1029/92GL01388

Reinen, L. A., Weeks, J. D., & Tullis, T. E. (1991). The frictional behavior of serpentinite: Implications for aseismic creep on shallow crustal faults. *Geophysical Research Letters*, *18*(10), 1921–1924. https://doi.org/10.1029/91GL02367

Ren, J., Xu, X., Zhang, G., Wang, Q., Zhang, Z., Gai, H., & Kang, W. (2022). Coseismic surface ruptures, slip distribution, and 3D seismogenic fault for the 2021 Mw 7.3 Maduo earthquake, central Tibetan Plateau, and its tectonic implications. *Tectonophysics*, *827*, 229275. https://doi.org/10.1016/j.tecto.2022.229275

Robertson, M. C., Sammis, C. G., Sahimi, M., & Martin, A. J. (1995). Fractal analysis of three-dimensional spatial distributions of earthquakes with a percolation interpretation. *Journal of Geophysical Research*, *100*(B1), 609–620. https://doi.org/10.1029/94JB02463

Rong, Y., Xu, X., Cheng, J., Chen, G., Magistrale, H., & Shen, Z.-K. (2020). A probabilistic seismic hazard model for Mainland China. *Earthquake Spectra*, *36*(1), 181–209. https://doi.org/10.1177/8755293020910754

Ross, Z. E., Idini, B., Jia, Z., Stephenson Oliver, L., Zhong, M., Wang, X., et al. (2019). Hierarchical interlocked orthogonal faulting in the 2019 Ridgecrest earthquake sequence. *Science*, *366*(6463), 346–351. https://doi.org/10.1126/science.aaz0109

Salditch, L., Stein, S., Neely, J., Spencer, B. D., Brooks, E. M., Agnon, A., & Liu, M. (2020). Earthquake supercycles and long-term fault memory. *Tectonophysics*, *774*, 228289. https://doi.org/10.1016/j.tecto.2019.228289

Savage, J. C. (1990). Equivalent strike-slip earthquake cycles in half-space and lithosphere-asthenosphere Earth models. *Journal of Geophysical Research*, *95*(B4), 4873–4879. https://doi.org/10.1029/JB095iB04p04873

Scholz, C. H. (1998). Earthquakes and friction laws. *Nature*, *391*(6662), 37–42. https://doi.org/10.1038/34097

Scholz, C. H. (2019). *The mechanics of earthquakes and faulting* (3rd ed.). Cambridge university press.

Scripps Institution Of Oceanography. (1986). *IRIS/IDA seismic network*. International Federation of Digital Seismograph Networks. https://doi.org/10.7914/SN/II

Shearer, P., Hauksson, E., & Lin, G. (2005). Southern California hypocenter relocation with waveform cross-correlation, Part 2: Results using source-specific station terms and cluster analysis. *Bulletin of the Seismological Society of America*, *95*(3), 904–915. https://doi.org/10.1785/0120040168

Shen, Z., Lü, J., Wang, M., & Bürgmann, R. (2005). Contemporary crustal deformation around the southeast borderland of the Tibetan Plateau. *Journal of Geophysical Research*, *110*(B11), B11409. https://doi.org/10.1029/2004JB003421

Shen, Z., Sun, J., Zhang, P., Wan, Y., Wang, M., Bürgmann, R., et al. (2009). Slip maxima at fault junctions and rupturing of barriers during the 2008 Wenchuan earthquake. *Nature Geoscience*, *2*(10), 718–724. https://doi.org/10.1038/ngeo636

Shimizu, K., Yagi, Y., Okuwaki, R., & Fukahata, Y. (2020). Development of an inversion method to extract information on fault geometry from teleseismic data. *Geophysical Journal International*, *220*(2), 1055–1065. https://doi.org/10.1093/gji/ggz496

Sieh, K., Jones, L., Hauksson, E., Hudnut, K., Eberhart-Phillips, D., Heaton, T., et al. (1993). Near-field investigations of the landers earthquake sequence, April to July 1992. *Science*, *260*(5105), 171–176. https://doi.org/10.1126/science.260.5105.171

Smalley, R., Ellis, M. A., Paul, J., & Van Arsdale, R. B. (2005). Space geodetic evidence for rapid strain rates in the New Madrid seismic zone of central USA. *Nature*, *435*(7045), 1088–1090. https://doi.org/10.1038/nature03642

Socquet, A., Hollingsworth, J., Pathier, E., & Bouchon, M. (2019). Evidence of supershear during the 2018 magnitude 7.5 Palu earthquake from space geodesy. *Nature Geoscience*, *12*(3), 192–199. https://doi.org/10.1038/s41561-018-0296-0

Socquet, A., Simons, W., Vigny, C., McCaffrey, R., Subarya, C., Sarsito, D., et al. (2006). Microblock rotations and fault coupling in SE Asia triple junction (Sulawesi, Indonesia) from GPS and earthquake slip vector data. *Journal of Geophysical Research*, *111*(B8), B08409. https://doi.org/10.1029/2005JB003963

Steacy, S., Gomberg, J., & Cocco, M. (2005). Introduction to special section: Stress transfer, earthquake triggering, and time-dependent seismic hazard. *Journal of Geophysical Research*, *110*(B5), B05S01. https://doi.org/10.1029/2005JB003692

Stein, R. S., Barka, A. A., & Dieterich, J. H. (1997). Progressive failure on the North Anatolian fault since 1939 by earthquake stress triggering. *Geophysical Journal International*, *128*(3), 594–604. https://doi.org/10.1111/j.1365-246X.1997.tb05321.x

Stein, S. (2007). New Madrid GPS: Much ado about nothing? *Eos, Transactions - American Geophysical Union*, *88*(5), 59. https://doi.org/10.1029/2007EO050008

Styron, R., & Pagani, M. (2020). The GEM global active faults database. *Earthquake Spectra*, *36*(1), 160–180. https://doi.org/10.1177/8755293020944182

Tadapansawut, T., Okuwaki, R., Yagi, Y., & Yamashita, S. (2021). Rupture process of the 2020 caribbean earthquake along the oriente transform fault, involving supershear rupture and geometric complexity of fault. *Geophysical Research Letters*, *48*(1), e2020GL090899. https://doi.org/10.1029/2020GL090899

Tapponnier, P., & Molnar, P. (1976). Slip-line field theory and large-scale continental tectonics. *Nature*, *264*(5584), 319–324. https://doi.org/10.1038/264319a0

Taylor, M., & Yin, A. (2009). Active structures of the Himalayan-Tibetan orogen and their relationships to earthquake distribution, contemporary strain field, and Cenozoic volcanism. *Geosphere*, *5*(3), 199–214. https://doi.org/10.1130/GES00217.1

Thatcher, W. (1993). The earthquake cycle and its role in the long-term deformation on the continental litosphere.

Thatcher, W. (2007). Microplate model for the present-day deformation of Tibet. *Journal of Geophysical Research*, *112*(B1), B01401. https://doi.org/10.1029/2005JB004244

Thomas, M. Y., Avouac, J.-P., Champenois, J., Lee, J.-C., & Kuo, L.-C. (2014). Spatiotemporal evolution of seismic and aseismic slip on the longitudinal valley fault, Taiwan. *Journal of Geophysical Research: Solid Earth*, *119*(6), 5114–5139. https://doi.org/10.1002/2013JB010603

Thomas, M. Y., Avouac, J.-P., Gratier, J.-P., & Lee, J.-C. (2014). Lithological control on the deformation mechanism and the mode of fault slip on the longitudinal valley fault, Taiwan. *Tectonophysics*, *632*, 48–63. https://doi.org/10.1016/j.tecto.2014.05.038

Thomas, M. Y., Avouac, J.-P., & Lapusta, N. (2017). Rate-and-state friction properties of the longitudinal valley fault from kinematic and dynamic modeling of seismic and aseismic slip. *Journal of Geophysical Research: Solid Earth*, *122*(4), 3115–3137. https://doi.org/10.1002/2016JB013615

University of Tokyo Earthquake Research Institute (Todai ERI Japan). (1989). Pacific21 (ERI/STA). Retrieved from https://www.fdsn.org/networks/detail/PS/

Walker, K. T., & Shearer, P. M. (2009). Illuminating the near-sonic rupture velocities of the intracontinental Kokoxili Mw 7.8 and Denali fault Mw 7.9 strike-slip earthquakes with global P wave back projection imaging. *Journal of Geophysical Research*, *114*(B2), B02304. https://doi.org/10.1029/2008JB005738

Wallace, L. M., McCaffrey, R., Beavan, J., & Ellis, S. (2005). Rapid microplate rotations and backarc rifting at the transition between collision and subduction. *Geology*, *33*(11), 857–860. https://doi.org/10.1130/G21834.1

Wallace, L. M., Stevens, C., Silver, E., McCaffrey, R., Loratung, W., Hasiata, S., et al. (2004). GPS and seismological constraints on active tectonics and arc-continent collision in Papua New Guinea: Implications for mechanics of microplate rotations in a plate boundary zone. *Journal of Geophysical Research*, *109*(B5), B05404. https://doi.org/10.1029/2003JB002481

Wang, H., Wright, T., & Biggs, J. (2009). Interseismic slip rate of the northwestern Xianshuihe fault from InSAR data. *Geophysical Research Letters*, *36*(3), L03302. https://doi.org/10.1029/2008GL036560

Wang, K., Zhu, Y., Nissen, E., & Shen, Z.-K. (2021). On the relevance of geodetic deformation rates to earthquake potential. *Geophysical Research Letters*, *48*(11), e2021GL093231. https://doi.org/10.1029/2021GL093231

Wang, M., & Shen, Z.-K. (2020). Present-day crustal deformation of continental China derived from GPS and its tectonic implications. *Journal of Geophysical Research: Solid Earth*, *125*(2), e2019JB018774. https://doi.org/10.1029/2019JB018774

Wang, M., Shen, Z.-K., Wang, Y.-Z., Bürgmann, R., Wang, F., Zhang, P.-Z., et al. (2021). Postseismic deformation of the 2008 Wenchuan earthquake illuminates lithospheric rheological structure and dynamics of eastern Tibet. *Journal of Geophysical Research: Solid Earth*, *126*(9), e2021JB022399. https://doi.org/10.1029/2021JB022399

Wang, M., Wang, F., Jiang, X., Tian, J., Li, Y., Sun, J., & Shen, Z.-K. (2021). GPS determined coseismic slip of the 2021 Mw7.4 Maduo, China, earthquake and its tectonic implication. *Geophysical Journal International*, *228*(3), 2048–2055. https://doi.org/10.1093/gji/ggab460

Wang, Q., Qiao, X., Lan, Q., Jeffrey, F., Yang, S., Xu, C., et al. (2011). Rupture of deep faults in the 2008 Wenchuan earthquake and uplift of the Longmen Shan. *Nature Geoscience*, *4*(9), 634–640. https://doi.org/10.1038/ngeo1210

Wang, R., Lorenzo-Martín, F., & Roth, F. (2006). PSGRN/PSCMP—A new code for calculating co- and post-seismic deformation, geoid and gravity changes based on the viscoelastic-gravitational dislocation theory. *Computers & Geosciences*, *32*(4), 527–541. https://doi.org/10.1016/j.cageo.2005.08.006

Wang, S., Song, C., Li, S., & Li, X. (2022a). Resolving co- and early post-seismic slip variations of the 2021 MW 7.4 Maduo earthquake in east Bayan Har block with a block-wide distributed deformation mode from satellite synthetic aperture radar data. *Earth and Planetary Physics*, *6*(1), 108–122. https://doi.org/10.26464/epp2022007

Wang, W., Fang, L., Wu, J., Tu, H., Chen, L., Lai, G., & Zhang, L. (2021). Aftershock sequence relocation of the 2021 MS7.4 Maduo earthquake, Qinghai, China. *Science China Earth Sciences*, *64*(8), 1371–1380. https://doi.org/10.1007/s11430-021-9803-3

Wang, W., He, J., Wang, X., Zhou, Y., Hao, J., Zhao, L., & Yao, Z. (2022). Rupture process models of the Yangbi and Maduo earthquakes that struck the eastern Tibetan Plateau in May 2021. *Science Bulletin*, *67*(5), 466–469. https://doi.org/10.1016/j.scib.2021.11.009

Wang, W., Qiao, X., & Ding, K. (2021). Present-day kinematics in southeastern Tibet inferred from GPS measurements. *Journal of Geophysical Research: Solid Earth*, *126*(1), e2020JB021305. https://doi.org/10.1029/2020JB021305

Wang, W., Qiao, X., Yang, S., & Wang, D. (2017). Present-day velocity field and block kinematics of Tibetan Plateau from GPS measurements. *Geophysical Journal International*, *208*(2), 1088–1102. https://doi.org/10.1093/gji/ggw445

Watson, A. R., Elliott, J. R., & Walters, R. J. (2022). Interseismic strain accumulation across the main recent fault, SW Iran, from Sentinel-1 InSAR observations. *Journal of Geophysical Research: Solid Earth*, *127*(2), e2021JB022674. https://doi.org/10.1029/2021JB022674

Webster, R., & Oliver, M. A. (2007). *Geostatistics for environmental scientists*. John Wiley Sons. Retrieved from https://planninginsights.co.in/data/ebook/1622466729.pdf

Wegnüller, U., Werner, C., Strozzi, T., Wiesmann, A., Frey, O., & Santoro, M. (2016). Sentinel-1 support in the GAMMA software. *Procedia Computer Science*, *100*, 1305–1312. https://doi.org/10.1016/j.procs.2016.09.246

Wei, S., Fielding, E., Leprince, S., Sladen, A., Avouac, J.-P., Helmberger, D., et al. (2011). Superficial simplicity of the 2010 El Mayor–Cucapah earthquake of Baja California in Mexico. *Nature Geoscience*, *4*(9), 615–618. https://doi.org/10.1038/ngeo1213

Weislogel, A. L. (2008). Tectonostratigraphic and geochronologic constraints on evolution of the northeast Paleotethys from the Songpan-Ganzi complex, central China. *Tectonophysics*, *451*(1), 331–345. https://doi.org/10.1016/j.tecto.2007.11.053

Weiss, J. R., Walters, R. J., Morishita, Y., Wright, T. J., Lazecky, M., Wang, H., et al. (2020). High-resolution surface velocities and strain for Anatolia from Sentinel-1 InSAR and GNSS data. *Geophysical Research Letters*, *47*(17), e2020GL087376. https://doi.org/10.1029/2020GL087376

Wells, D. L., & Coppersmith, K. J. (1994). New empirical relationships among magnitude, rupture length, rupture width, rupture area, and surface displacement. *Bulletin of the Seismological Society of America*, *84*(4), 974–1002. https://doi.org/10.1785/BSSA0840040974

Wen, X., Yi, G., & Xu, X. (2007). Background and precursory seismicities along and surrounding the Kunlun fault before the Ms8.1, 2001, Kokoxili earthquake, China. *Journal of Asian Earth Sciences*, *30*(1), 63–72. https://doi.org/10.1016/j.jseaes.2006.07.008

Wen, Y.-Y., & Ma, K.-F. (2010). Fault geometry and distribution of asperities of the 1997 Manyi, China (Mw = 7.5), earthquake: Integrated analysis from seismological and InSAR data. *Geophysical Research Letters*, *37*(5), L05303. https://doi.org/10.1029/2009GL041976

Wesnousky, S. G. (1988). Seismological and structural evolution of strike-slip faults. *Nature*, *335*(6188), 340–343. https://doi.org/10.1038/335340a0

Wessel, P., Smith, W. H. F., Scharroo, R., Luis, J., & Wobbe, F. (2013). Generic mapping tools: Improved version released. *Eos, Transactions American Geophysical Union*, *94*(45), 409–410. https://doi.org/10.1002/2013EO450001

Wesson, R. L. (1988). Dynamics of fault creep. *Journal of Geophysical Research*, *93*(B8), 8929–8951. https://doi.org/10.1029/JB093iB08p08929

Wright, T. J. (2016). The earthquake deformation cycle. *Astronomy and Geophysics*, *54*(7), 4.20–4.26. https://doi.org/10.1093/astrogeo/atw148

Wright, T. J., Elliott, J. R., Wang, H., & Ryder, I. (2013). Earthquake cycle deformation and the Moho: Implications for the rheology of continental lithosphere. *Tectonophysics*, *609*, 504–523. https://doi.org/10.1016/j.tecto.2013.07.029

Xiong, X., Shan, B., Zheng, Y., & Wang, R. (2010). Stress transfer and its implication for earthquake hazard on the Kunlun Fault, Tibet. *Tectonophysics*, *482*(1), 216–225. https://doi.org/10.1016/j.tecto.2009.07.020

Xu, M., Zhu, C., Rao, S., & Hu, S. (2011). Difference of thermal structure between eastern edge of Tibetan Plateau and western Sichuan Basin. *Chinese Journal of Geology*, *46*(1), 203–212.

Xu, X.-W., Chen, G.-H., Wang, Q.-X., Chen, L.-C., Ren, Z.-K., Xu, C., et al. (2017). Discussion on seismogenic structure of Jiuzhaigou earthquake and its implication for current strain state in the southeastern Qinghai-Tibet Plateau. *Chinese Journal of Geophysics*, *60*(10), 4018–4026. https://doi.org/10.6038/cjg20171028

Yabuki, T., & Matsu'ura, M. (1992). Geodetic data inversion using a Bayesian information criterion for spatial distribution of fault slip. *Geophysical Journal International*, *109*(2), 363–375. https://doi.org/10.1111/j.1365-246X.1992.tb00102.x

Yagi, Y., & Fukahata, Y. (2011). Introduction of uncertainty of Green's function into waveform inversion for seismic source processes. *Geophysical Journal International*, *186*(2), 711–720. https://doi.org/10.1111/j.1365-246X.2011.05043.x

Yamashita, S., Yagi, Y., Okuwaki, R., Shimizu, K., Agata, R., & Fukahata, Y. (2021). Consecutive ruptures on a complex conjugate fault system during the 2018 Gulf of Alaska earthquake. *Scientific Reports*, *11*(1), 5979. https://doi.org/10.1038/s41598-021-85522-w

Yao, W., Wang, Z., Liu-Zeng, J., Liu, X., Han, L., Shao, Y., et al. (2022). Discussion on coseismic surface rupture length of the 2021 Mw 7.4 Madoi earthquake, Qinghai, China. *Seismology and Geology*, *44*(2), 541–559. https://doi.org/10.3969/j.issn.0253-4967.2022.02.016

Yu, C., Li, Z., & Penna, N. T. (2020). Triggered afterslip on the southern Hikurangi subduction interface following the 2016 Kaikōura earthquake from InSAR time series with atmospheric corrections. *Remote Sensing of Environment*, *251*, 112097. https://doi.org/10.1016/j.rse.2020.112097

Yu, C., Li, Z., Penna, N. T., & Crippa, P. (2018). Generic atmospheric correction model for interferometric synthetic aperture radar observations. *Journal of Geophysical Research: Solid Earth*, *123*(10), 9202–9222. https://doi.org/10.1029/2017JB015305

Yue, H., Shen, Z.-K., Zhao, Z., Wang, T., Cao, B., Li, Z., et al. (2022). Rupture process of the 2021 M7.4 Maduo earthquake and implication for deformation mode of the Songpan-Ganzi terrane in Tibetan Plateau. *Proceedings of the National Academy of Sciences*, *119*(23), e2116445119. https://doi.org/10.1073/pnas.2116445119

Zhan, Y., Liang, M., Sun, X., Huang, F., Zhao, L., Gong, Y., et al. (2021). Deep structure and seismogenic pattern of the 2021.5.22 Madoi (Qinghai) Ms7.4 earthquake. *Chinese Journal of Geophysics*, *64*(7), 2232–2252. https://doi.org/10.6038/cjg2021O0521

Zhang, G., Ma, H., Wang, H., & Li, L. (2004). The relationship between active blocks and strong earthquakes in mainland China. *Science China Earth Sciences*, *7*, 591–599.

Zhang, P., Deng, Q., Zhang, G., Ma, J., Gan, W., Min, W., et al. (2003). Strong earthquakes and active blocks in mainland China. *Science in China, Series A D*, *33*(B04), 12–20.

Zhang, P.-Z. (2013a). Beware of slowly slipping faults. *Nature Geoscience*, *6*(5), 323–324. https://doi.org/10.1038/ngeo1811

Zhang, P.-Z. (2013b). A review on active tectonics and deep crustal processes of the Western Sichuan region, eastern margin of the Tibetan Plateau. *Tectonophysics*, *584*, 7–22. https://doi.org/10.1016/j.tecto.2012.02.021

Zhang, P.-Z., Shen, Z., Wang, M., Gan, W., Bürgmann, R., Molnar, P., et al. (2004). Continuous deformation of the Tibetan Plateau from global positioning system data. *Geology*, *32*(9), 809–812. https://doi.org/10.1130/G20554.1

Zhang, Q., Wu, Y., Guo, N., & Chen, C. (2022a). Research on deformation characteristics of the 2021 Qinghai Maduo MS7.4 earthquake through coseismic dislocation inversion. *Advances in Space Research*, *69*(8), 3059–3070. https://doi.org/10.1016/j.asr.2022.01.042

Zhang, X., Feng, W., Du, H., Samsonov, S., & Yi, L. (2022). Supershear rupture during the 2021 MW 7.4 Maduo, China, earthquake. *Geophysical Research Letters*, *49*(6), e2022GL097984. https://doi.org/10.1029/2022GL097984

Zhao, D., Qu, C., Bürgmann, R., Shan, X., Li, T., Li, C., et al. (2022). Deep, shallow and surface fault-zone deformation during and after the 2021 Mw7.4 Maduo, Qinghai, earthquake illuminates fault structural immaturity [Preprint]. ESSOAr. https://doi.org/10.1002/essoar.10511891.1

Zhao, D., Qu, C., Chen, H., Shan, X., Song, X., & Gong, W. (2021). Tectonic and geometric control on fault kinematics of the 2021 Mw7.3 Maduo (China) earthquake inferred from interseismic, coseismic, and postseismic InSAR observations. *Geophysical Research Letters*, *48*(18), e2021GL095417. https://doi.org/10.1029/2021GL095417

Zheng, G., Wang, H., Wright, T. J., Lou, Y., Zhang, R., Zhang, W., et al. (2017). Crustal deformation in the India-Eurasia collision zone from 25 years of GPS measurements. *Journal of Geophysical Research: Solid Earth*, *122*(11), 9290–9312. https://doi.org/10.1002/2017JB014465

Zhu, L., Ji, L., & Liu, C. (2021). Interseismic slip rate and locking along the Maqin–Maqu segment of the east Kunlun Fault, northern Tibetan Plateau, based on Sentinel-1 images. *Journal of Asian Earth Sciences*, *211*, 104703. https://doi.org/10.1016/j.jseaes.2021.104703

Zhu, Y., Diao, F., Fu, Y., Liu, C., & Xiong, X. (2021). Slip rate of the seismogenic fault of the 2021 Maduo earthquake in western China inferred from GPS observations. *Science China Earth Sciences*, *64*(8), 1363–1370. https://doi.org/10.1007/s11430-021-9808-0

Zhu, Y., Wang, K., & He, J. (2020). Effects of earthquake recurrence on localization of interseismic deformation around locked strike-slip faults. *Journal of Geophysical Research: Solid Earth*, *125*(8), e2020JB019817. https://doi.org/10.1029/2020JB019817